POWER BEAMING WITH C-SI PHOTOVOLTAIC CELLS

A THESIS SUBMITTED TO
THE GRADUATE SCHOOL OF NATURAL AND APPLIED SCIENCES
OF
MIDDLE EAST TECHNICAL UNIVERSITY

BY

ŞAFAK VACİT AÇIKGÖZ

IN PARTIAL FULFILLMENT OF THE REQUIREMENTS
FOR
THE DEGREE OF MASTER OF SCIENCE
IN
PHYSICS

MARCH 2025

Approval of the thesis:

POWER BEAMING WITH C-SI PHOTOVOLTAIC CELLS

submitted by **ŞAFAK VACİT AÇIKGÖZ** in partial fulfillment of the requirements for the degree of **Master of Science** i**n Physics, Middle East Technical University** by,

Prof. Dr. Naci Emre Altun
Dean, **Graduate School of Natural and Applied Sciences** _____

Prof. Dr. Seçkin Kürkçüoğlu
Head of the Department, **Physics** _____

Assist. Prof. Dr. Ihor Pavlov
Supervisor, **Physics, METU** _____

Examining Committee Members:

Assist. Prof. Dr. Parviz Elahi
Natural and Mathematical Sciences, Özyeğin University _____

Assist. Prof. Dr. Ihor Pavlov
Physics, METU _____

Prof. Dr. Ahmet Bingül
Engineering of Physics, Gaziantep University _____

Date: 13.03.2025

I hereby declare that all information in this document has been obtained and presented in accordance with academic rules and ethical conduct. I also declare that, as required by these rules and conduct, I have fully cited and referenced all material and results that are not original to this work.

Name Last name : Şafak Vacit Açıkgöz

Signature :

ABSTRACT

POWER BEAMING WITH C-SI PHOTOVOLTAIC CELLS

Açıkgöz, Şafak Vacit
Master of Science, Physics
Supervisor : Assist. Prof. Dr. Ihor Pavlov

March 2025, 96 pages

Transferring energy wirelessly has long been a dream of humanity. One popular way in the past few years is power beaming which can be defined as transferring energy wirelessly via electromagnetic radiation. It can be used for many applications: Unmanned aerial vehicles (UAV) that do not need to land for refueling, electric cars that do not need recharging, providing electricity to remote areas without the costly infrastructure, biomedical devices that can work wirelessly. There are various wavelengths to choose for a power source and different types of receivers. Infrared is advantageous in the long range for having a well collimated beam and having an atmospheric window. The present studies focus on GaAs or other costly III-V materials not common in the industry. However, silicon is a more widely accessible, economic and abundant material which is well-studied, making it a favorable receiver material choice. The present industrial infrastructure of silicon solar cells makes it economically feasible to produce photovoltaic (PV) receivers on a large scale. This study aims at building a wavelength-tunable fiber laser in the range 1030-1080 nm that can provide more than 50 W of optical power for harvesting energy with a PV receiver from a monochromatic light source, laser beam. For the characterization of the PV receivers, a custom built current-voltage (IV) measurement system has been designed and characterized by their efficiency at maximum power points (MPP) under different illuminations. Optimization on

different monofacial and bifacial Passivated Emitter and Rear Contact (PERC) cells was done by simulation. They were fabricated and experimented with along Interdigitated Back Contact (IBC) cells. The goal was to find the optimal beam parameters and the receiver PV cell design with the highest efficiency.

Keywords: Power beaming, Wireless energy transmission, Solar cell, Crystalline silicon (c-Si) photovoltaic elements.

ÖZ

C-Sİ FOTOVOLTAİK HÜCRELER İLE OPTİK GÜÇ AKTARIMI

Açıkgöz, Şafak Vacit
Yüksek Lisans, Fizik
Tez Yöneticisi: Dr. Öğr. Üyesi Ihor Pavlov

Mart 2025, 96 sayfa

Kablosuz enerji aktarımı uzun zamandır insanlığın hayallerinden biri olagelmiştir. Son yıllarda popüler hale gelen yöntemlerden biri, elektromanyetik radyasyon yoluyla enerjiyi kablosuz olarak aktarmayı sağlayan optik güç aktarımıdır (Power Beaming). Bu teknolojinin, birçok uygulamada kullanımı mümkündür: Yakıt ikmali için iniş yapmasına gerek olmayan insansız hava araçları (İHA), şarj gerektirmeyen elektrikli araçlar, pahalı altyapıya ihtiyaç duymadan uzak bölgelere elektrik sağlanması ve kablosuz olarak çalışabilen biyomedikal cihazlar. Enerji kaynağı olarak farklı dalga boyları ve çeşitli alıcı türleri arasından seçim yapılabilir. Kızılötesi ışınlar, iyi kolime edilebilmesi ve atmosferik bir pencereye sahip olması nedeniyle uzun mesafelerde avantajlıdır. Günümüzde yapılan çalışmalar genellikle GaAs veya sanayide yaygın olarak bulunmayan, pahalı III-V grubu malzemelere odaklanmaktadır. Ancak, silisyum (Si) daha yaygın, ekonomik ve bol bulunan bir malzeme olup, üzerine yapılan araştırmalar oldukça kapsamlıdır. Bu da onu avantajlı bir alıcı materyali adayı yapmaktadır. Silisyum güneş hücrelerinin mevcut endüstriyel altyapısı, fotovoltaik (PV) alıcıların büyük ölçekli üretimini ekonomik olarak makul kılmaktadır. Bu çalışmanın amacı, 1030-1080 nm aralığında dalgaboyu ayarlanabilen ve 50 W'dan fazla optik güç sağlayabilen bir fiber lazerin inşasıyla monokromatik ışık kaynağı, lazer ışınından, bir fotovoltaik (FV) hücre ile enerji elde

etmektir. FV hücrelerin karakterizasyonu için özel yapım bir akım-voltaj (IV) ölçüm sistemi tasarlanmıştır ve en yüksek güç noktasındaki (MPP) verimine göre karakterizasyonları yapılmıştır. Farklı monofacial ve bifacial Passivated Emitter and Rear Contact (PERC) hücreleri üzerinde optimizasyon çalışmaları simülasyonlarla gerçekleştirilmiş, ardından üretilerek Interdigitated Back Contact (IBC) hücreleri ile birlikte deneyler yapılmıştır. Hedef, en yüksek verimliliği sağlayacak en uygun ışın parametrelerini ve PV alıcı hücre tasarımını belirlemektir.

Anahtar Kelimeler: Optik güç aktarımı (power beaming), Kablosuz enerji aktarımı, Güneş hücresi, Kristal silisyum (c-Si) fotovoltaik elemanlar.

ACKNOWLEDGMENTS

I would like to thank my supervisor Prof. Ihor Pavlov and Dr. Arian Goodarzi for all they have taught me about optics and fiber laser systems over the years. Special thanks to Prof. Pavlov for always finding a solution in all the challenges we have faced throughout this study. Also special thanks to Dr. Khalil Dadashi, fellow researcher in this project, for being my co-advisor and all his help throughout the project. His suggestions to the thesis work and academic advices were of great importance.

I would like to thank Prof. Ahmet Bingül for all his support and suggestions and Prof. Parviz Elahi for his suggestions. Also special thanks to Prof. Güven Çankaya for his advices and support throughout my studies.

I would like to thank Basil Aldeeb for his help on building the electronics measurement system used in this study.

I would like to thank my family for their life long support and all my friends that have supported me.

I would like to thank the Center for Solar Energy Research and Applications (ODTÜ-GÜNAM) for enabling the use of their facilities for photovoltaic cell fabrication.

I would like to thank Scientific and Technological Research Council of Turkey (TUBITAK) for funding this work under grant number TUBITAK 121F282.

TABLE OF CONTENTS

LIST OF TABLES

TABLES

LIST OF FIGURES

FIGURES

LIST OF ABBREVIATIONS

ABBREVIATIONS

ADC	Analog to Digital Converter
APC	Angled Physical Contact
BD	Beam Diameter
BDAF	Beam Diameter at the Focus Point
c-Si	Crystalline Silicon
CW	Continuous Wave
DC	Direct Current
DC-DC	Direct Current to Direct Current
DC PM	Double-Clad Polarization Maintaining
EM	Electromagnetic
FWHM	Full Width at Half Maximum
GaAs	Gallium Arsenide
GaInP	Gallium Indium Phosphate
IBC	Interdigitated Back Contact
IMD	Implantable/Ingestible Medical Device
I_{sc}	Short-circuit Current
IV	Current-Voltage
LPT	Laser Power Transfer
MAPLE	Microwave Array Power Transfer LEO Experiment

MM	Multi-Mode
MPC	Multi-Mode Pump Combiner
MPP	Maximum Power Point
NI	National Instruments
OSA	Optical Spectrum Analyzer
OWC	Optical Wireless Communication
OWPT	Optical Wireless Power Transfer
PC	Personal Computer
PERL	Passivated Emitter Rear Locally-diffused
PERC	Passivated Emitter and Rear Contact
PLD	Pump Laser Diode
PM	Polarization Maintaining
PWM	Pulse Width Modulation
RF	Radio Frequency
RTG	Radioisotope Thermoelectric Generator
SC	Solar Cell
SSPS	Space Solar Power Satellite/Station
SWIR	Short-wave Infrared
UAV	Unmanned Aerial Vehicle
UWOC	Underwater Wireless Optical Communication
VDC	Direct Current Voltage
VMJ	Vertical Multi-Junction

V_{oc}	Open-circuit Voltage
Yb	Ytterbium

CHAPTER 1

INTRODUCTION

The ability to transfer energy has always been essential for fulfilling humanity's energy needs. This necessity arises because energy sources are often located far from the point of consumption. Research on wireless energy transfer has been ongoing since Nikola Tesla's work over a century ago [1]. In recent years, wireless energy transfer has emerged as a transformative technology with potential applications across multiple domains, including terrestrial, aerial, underwater, space, and everyday applications.

Several examples illustrate its wide-ranging impact. On land, wireless energy transfer could enable electric vehicles to operate continuously without stopping at charging stations [2] and allow electronic devices, such as smartphones, to charge automatically upon entering a room [3]. In the air, it could support perpetually flying vehicles that do not require landing for refueling [4] and provide electricity to remote areas without the need for costly infrastructure. In space, solar power collected by orbiting solar panels could be transmitted continuously to any location on Earth, independent of weather conditions [5]. In biomedical applications, wireless power could energize implanted medical devices, eliminating the need for surgical battery replacements [6].

Although power beaming research has existed for decades, significant advancements have occurred only in the past two decades. The number of annual publications on this topic has steadily increased since 2000, with a dramatic rise after 2010 [7]. This growth is largely driven by technological improvements, which have made power beaming more efficient and economically viable. In particular, the rapid expansion

of the solar industry has accelerated advancements in semiconductor laser diodes and photovoltaic technology, laying the groundwork for power beaming applications [8].

Power beaming includes a transmitter and a receiver for utilizing the transferred energy. Power beaming can be achieved using transmitters operating at various wavelengths. In this study, an infrared source (a wavelength-tunable fiber laser) serves as the transmitter, while silicon-based photovoltaic receivers—including monofacial and bifacial Passivated Emitter and Rear Contact (PERC) and Interdigitated Back Contact (IBC) cells—act as energy converters. These choices offer several advantages.

On the transmitter side, infrared fiber lasers can generate well-collimated beams capable of carrying high power over long distances. Additionally, advancements in semiconductor diode technology, driven by the solar industry, have made the pump diodes needed for infrared fiber lasers increasingly cost-effective.

On the receiver side, silicon's bandgap is well-matched to the photon energy of short-wave infrared (SWIR) light, enabling high theoretical efficiency with minimal energy loss. Moreover, silicon photovoltaic cells are significantly more cost-effective than alternatives like gallium arsenide (GaAs) or indium gallium phosphide (InGaP) due to their widespread use in commercial applications such as solar panels, computer processors, and laser diodes. While III-V semiconductor materials are often explored in power beaming research, their high production costs and limited manufacturing infrastructure make them less practical for large-scale deployment. In contrast, silicon-based materials benefit from an established global supply chain, reducing production costs and improving scalability. Furthermore, silicon has been extensively studied for solar applications, and its well-documented properties can be leveraged for power beaming. It is also the second most abundant element in Earth's crust, making it a sustainable, efficient, and economically viable option for large-scale power beaming applications [9].

This study examines the behavior of monofacial and bifacial PERC photovoltaic cells in the SWIR range (1030–1080 nm). To achieve this, a wavelength-tunable

fiber laser capable of delivering over 50W of optical power was developed. The laser system is designed to be portable, enabling outdoor experiments for long-distance power beaming applications.

A novel thin multi-cell bifacial PERC design was implemented by fabricating and stacking thin bifacial PERC cells oriented toward the laser beam. The performance of these photovoltaic receivers was characterized through current-voltage (IV) measurements using a custom-built measurement system.

After this introductory chapter, the thesis is organized as follows; in the second chapter, historical overview of power beaming was presented and the contributions of this study is outlined.

In the third chapter, the theoretical foundations of power beaming, including the mechanisms of energy conversion in photovoltaic receivers and the efficiency limit is explained. Also, the wavelength ranges with their advantages are being discussed for different power beaming purposes.

In the fourth chapter, infrared fiber laser used in this study and the novel thin multi-cell design is presented. It also describes the optimization of wire grid spacing using Griddler Pro simulations, the fabrication process following the simulations.

Then in the fifth chapter, the experimental results obtained from thin multi-cell design and IBC cells are presented and analyzed along with a discussion of PV panel performance and future research directions. Alternative approaches, such as multi-beam configurations, are also evaluated.

CHAPTER 2

LITERATURE REVIEW

The definition of power beaming can vary depending on the context it is used. The basic concept of power beaming is the transfer of energy wirelessly via electromagnetic (EM) waves. This covers all of the transmitters producing any wavelength of EM wave, including visible light, infrared, microwave and terahertz ranges. However, the term is generally used interchangeably with “laser power beaming”, which specifies the transmitter beam to be originating from a laser source. This study will also be specifically focusing on laser power beaming due to its superior capabilities regarding long-range terrestrial applications which are explained in more detail in the next sub-sections. Firstly, the early development stages of power beaming are presented which covers the work until the year 2001. This part includes both microwave and laser power beaming studies whose total number is very few nevertheless. Then the second section covers the studies done after 2001 until 2021 but focusing on laser power beaming only. The third, fourth, fifth and sixth sections present the studies until present day, each focusing on a specific application area, respectively; Space, Underwater, Daily Life and Laser Power Converters.

2.1 History of Power Beaming

2.1.1 Early Power Beaming Studies

It was around the 1900s when Nikola Tesla made his outstanding work on wireless power transmission [1]. However, the practical demonstrations of power beaming

emerged much later from Tesla's time. After microwave technology advancing in World War II, in 1964, William C. Brown conducted pioneering experiments to transport energy from one location to another using microwave technology. He explored the feasibility of transmitting energy via microwave beams generated in high-power microwave tubes capable of providing continuous power at a wavelength of 10 cm [10].

In 1965 Brown's group demonstrated the first system to wirelessly power an electric helicopter using microwaves [11]. In 1968 Peter E. Glaser introduced the concept of space-based solar power (SBSP) as a potential solution to Earth's energy challenges. He proposed deploying large-scale solar collectors in geostationary orbit to harness solar energy continuously, unaffected by atmospheric conditions or the day-night cycle. This energy would be converted into microwave beams and transmitted to ground-based receiving stations, known as rectennas, which would then convert the microwaves back into electricity for distribution. Glaser discussed the technological feasibility of this concept, including the design of the satellite systems and the means of energy transmission. He also addressed potential environmental impacts and the economic considerations of developing such a system. Glaser's visionary proposal laid the groundwork for subsequent research and development in the field of space-based solar power [12] which held a very critical role for a 2023 demonstration of beaming power from a satellite on orbit to a location on Earth [13] as will be explained in the space applications of power beaming within the next sections of this chapter.

In 1970, at Marshall Space Flight Center, a demonstration of microwave power beaming with higher efficiencies (rising from 13% in the older demonstration to 26% in this demonstration) was achieved and then 48% and later 54% in 1975 [14]. A gradual increase is seen in the efficiency of power beaming as the rectenna technology develops. The concept of SBSP later led to the demonstration of transferring 30 kW of power over a 1.6 km distance with microwaves in 1975 [14]. This demonstration has convinced many skeptics about the validity of power

beaming technology especially by using microwaves. With more attraction on microwave power beaming, efficiencies of 91% was achieved in 1976 [14].

In 1983, the program called Stationary High Altitude Relay Platform (SHARP) was sponsored by the Canadian Communication Research Center. In 1987, they have demonstrated a free-flying microwave-powered airplane that has a circular rectenna mounted beneath the wings [14] whose image can be seen in Figure 2.1. It had a 4.3 m wingspan, launched by hand, and reached an altitude of 100 m with the aid of a battery, later the battery was switched off and the plane kept its motion with power beaming only. The microwave beam was automatically kept focused on the rectenna which is distributed beneath the wings on a circular disk.

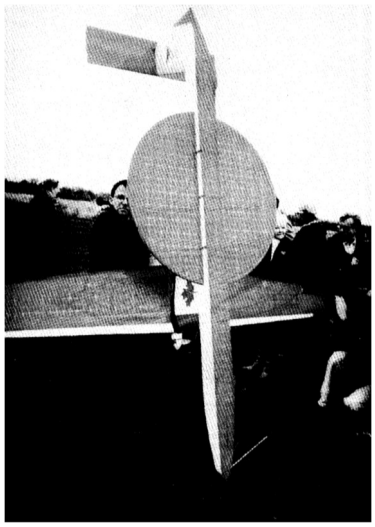

Figure 2.1. The demonstration of Canadian Communications Research Center of a power beamed airplane which received all the power needed for its propulsion in air from a microwave beam in 1987 [14]

In 1983, there is another major advancement in microwave power beaming, which is the design of an electronically steered phased array. Olaf T. von Ramm and Stephen W. Smith examined the principles and techniques for phased array beam steering. They analyzed how linear arrays can be utilized to steer and focus beams effectively during both transmission and reception phases. With a phased array, there

is no need to physically rotate the transmitter while steering the beam to follow the receiver. By only adjusting the phase of individual microwave sources (subarrays), the resultant microwave beam can be shaped and focused with no moving mechanical parts. This enables a much effective targeting of the transmitter beam for power beaming purposes [15].

In 1992, Martin Green, with his colleagues, demonstrated 45.1% optical to electrical efficiency by using Passivated Emitter Rear Locally Diffused (PERL) silicon photovoltaic cells under 1020 nm monochromatic light from a laser [16]. Although the intensity was relatively low for high power applications ($1W/cm^2$), this was one of the first studies achieving high efficiency with silicon solar cells under monochromatic light, contributing to the newly developing area of optical power beaming. At the time, microwave power beaming having a noticeable literature, laser power beaming (or optical power beaming) was newly being investigated.

Martin Green, in his 2001 paper, explained with its thermodynamic basis, that while solar photovoltaic systems have relatively low conversion efficiencies, thermodynamically it is possible to achieve efficiencies arbitrarily close to 100% by using monochromatic light [17].

2.1.2 A Sharp Increase in Power Beaming Studies

The studies on power beaming have continued gradually, however, from the 1980s until 2000s there were only a few dozen articles per year [7] but after 2000s, there is an increase in the number of articles per year. After 2010 a dramatic increase is seen. This is due to the developments in semiconductor industry. Both the advancements in high power semiconductor lasers and the growing solar market in the world leading to advancements in photovoltaic cell technology have made laser power beaming a feasible area of research and development [8].

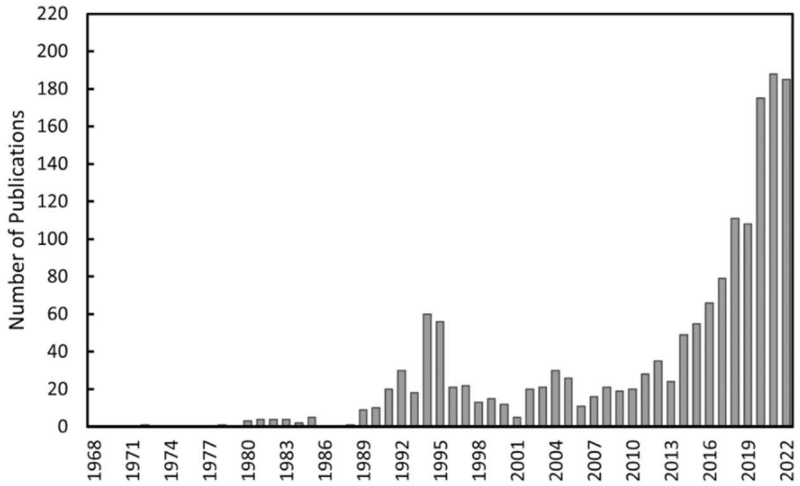

Figure 2.2. Number of publications related to OWPT. Nearly all data are based on the search keywords of "optical wireless power transmission" OR "optical wireless power transfer" OR "wireless optical power transmission" OR "laser wireless power transmission" OR "laser wireless power transfer" OR "wireless laser power transmission" OR "laser power beaming" in Google Scholar [7]

In 2002, researchers from European Aeronautic Defence and Space Company (EADS) built a rover powered by a 532 nm laser capable of providing 5 W of optical power and demonstrated driving the rover with power beaming while obtaining 20% optical to electrical efficiency with the GaInP photovoltaic cells mounted to the rover [18].

In 2005, a model plane is powered with laser light. Solar cells were suspended from a lightweight model airplane. The model plane was operated with a remote control while the laser beam was directed on the plane manually by hand, the laser was mounted on a rotating stage [19].

In 2006, at Kinki University, a kite and in 2008 a small helicopter (multicopter) was flown with power beaming (Figure 2.3). An 808 nm high-power fiber-coupled laser was used, producing 200 W optical power along with GaAs photovoltaic cell pieces connected in series and parallel, generating 42 W of electrical power [20]. Thus, its optical to electrical efficiency is 21%. The kite has flown for more than 1 hour and

the helicopter for several 10 minutes which weighed more than 1 kg while at the same time transmitting images wirelessly by a camera mounted on it.

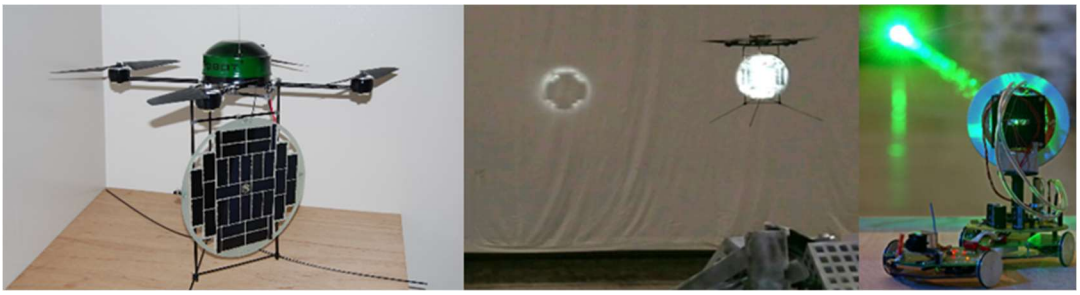

Figure 2.3. Multicopter powered by laser at Kinki University in 2008 (on the left and middle) [20], laser-powered rover developed by EADS (on the right) [21]

In 2009, LaserMotive (the first winner of NASA Space Elevator Challenge) made a quadcopter flight demo with Ascending Technologies GmbH. They have flown a quadcopter for more than 12 hours which has the battery capacity of 5 minutes if not charged with power beaming. They used a 810 nm laser capable of providing 1 kW optical power for beaming the GaAs photovoltaic cells mounted on the quadcopter, raising its temperature to 63 degrees Celsius [4]. Image of the drone can be seen in Figure 2.4 with the laser being incident from the bottom of the drone. The red beam seen at the center is for motion tracking and the pink light is the IR laser beam which carries the power that is charging the drone. IR is not visible to human eye but on the camera, imaging IR is possible and the software of most of the cameras assign a pink color to IR wavelengths.

In 2014, researchers at Beijing University of Technology have transferred 9.7 W power using 24 W of 793 nm laser light directed at a GaAs cell placed 100 m away [22]. They achieved 40.4% efficiency when optical power was 24 W and 48.4% at 8 W reaching peak efficiency.

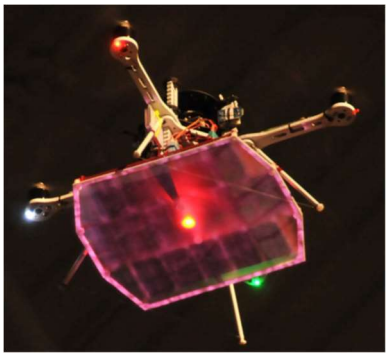

Figure 2.4. The drone from LaserMotive's 12 h power beaming demonstration [4]

In 2019, U.S. Naval Research Laboratory (NRL) made a demonstration of delivering 2 kW of power over 325 m, harvesting 400 W of it by photovoltaic cells and powering some household devices with it [23]. This implies achieving 20% efficiency. The wavelength regime of the laser is stated to be infrared, the exact wavelength or the photovoltaic cell type was not specified.

In 2021, telecom company Ericsson and PowerLight (formerly LaserMotive) has demonstrated world's first wirelessly powered 5 G station with the 100 W of power delivered over 300 m [24].

Again in 2021, researchers from Korea have demonstrated prolonging the flight duration of a DJI Tello micro-size drone with VMJ PV cells mounted on it and 976 nm 10 W laser source [25]. Their paper has provided an extensive study on the relationship of power beaming and flight time duration.

It was also investigated in a 2021 study whether power beaming can be feasible for recharging automobiles, its advantages and disadvantages with respect to other wireless energy transfer methods such as induction or radio frequency [2]. The evaluation in the paper suggested that optical power beaming is not recommended for powering electric vehicles on ground but better fitting for aerial vehicles. However, it was also stated that under conditions in which human interaction is less or some other specific conditions, still power beaming can be applied to electric vehicles on the road as well. The power beaming of ground vehicles is much more feasible in space missions. This is discussed with more detail in the next section.

2.1.3 Space Applications of Power Beaming

In addition to the many terrestrial and aerial applications, power beaming also has space applications. The space applications can be mainly divided into two categories; Space Solar Power Satellite/Station (SSPS) systems, and power replenishment of space exploration vehicles.

SSPS systems consist of harvesting solar energy in space via photovoltaic cells and transferring the harvested energy to any desired location on Earth via power beaming. This is possible by placing the solar panels in geosynchronous earth orbit (GEO) [5].

The main advantage of this is the access to solar energy 24/7, whenever needed, wherever needed with solar panels of area less than the amount required on land. It has the capability of directing the harvested power instantaneously to different receiver stations on Earth that can even be on different continents. This enables the efficient usage of power that has been generated in excess with respect to the energy needs of a specific area and redirect that excess power to a location where it can be utilized. There are many different designs proposed for the solar arrays that will be converting solar energy to electrical energy [26-29]. Some of the designs can be seen in Figure 2.5. Due to the disadvantage of having the need to large financial and technical investment required up front to carry a great number of solar panels into

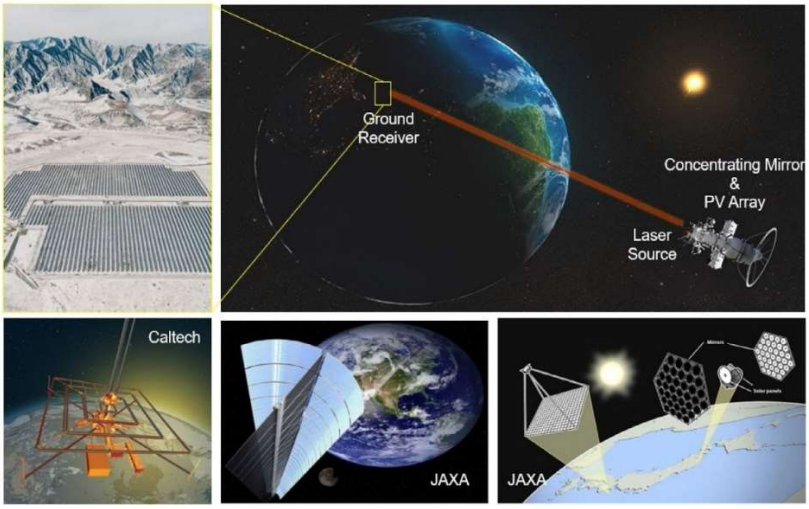

Figure 2.5. Various SSPS designs that were proposed over the years[30]

orbit, there have been new designs proposed that involve focusing of the sun light to a smaller area of arrays which are folded before take-off and gets unfolded after getting into orbit. This can save the amount of mass needed to carry to space, thus, decreasing the cost of space solar energy. The importance of the role of solar laser technology as a pivotal element in advancing sustainable and renewable energy has been emphasized in a 2024 study [31]. An illustration from the study can be seen in Figure 2.6.

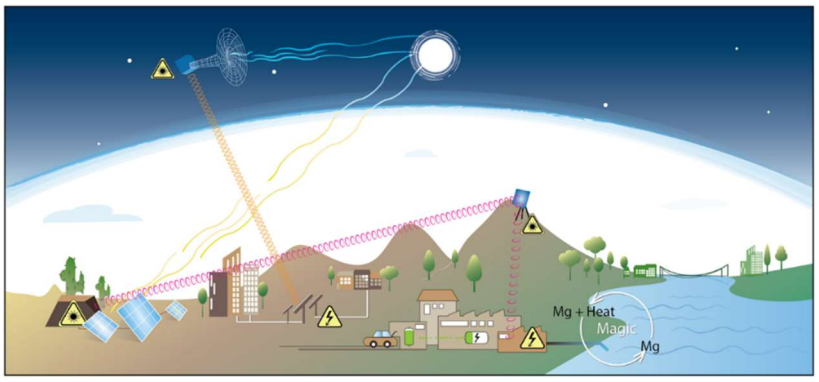

Figure 2.6. Graphical abstract representing the selected application of solar lasers for sustainable energy generation and optical communication [31]

However, the design stage is still ongoing, none of these proposed photovoltaic array designs have been built and tested in real life. On the other hand, a demonstration of beaming power to Earth from space has been established by Caltech researchers led by Ali Hajimiri on July 2023 [13]. This work was within the scope of MAPLE

(Microwave Array Power Transfer LEO Experiment), an experiment to verify the ability of space solar arrays to transmit energy in space and to evaluate their strengths and weaknesses.

Their goal is to use a phased array [12] to focus and change the focus of the RF beam with no moving parts. In this experiment, MAPLE was scheduled to turn on, steer power out the sapphire window opposite the array in space, and maintain its state for several minutes while passing over Pasadena following its orbit in space.

It has transferred a power of maximum 250 mW for less than 10 minutes to the ground station used for detection during the experiment located on the roof of Caltech's Moore Laboratory. Images from the study can be seen in Figure 2.7.

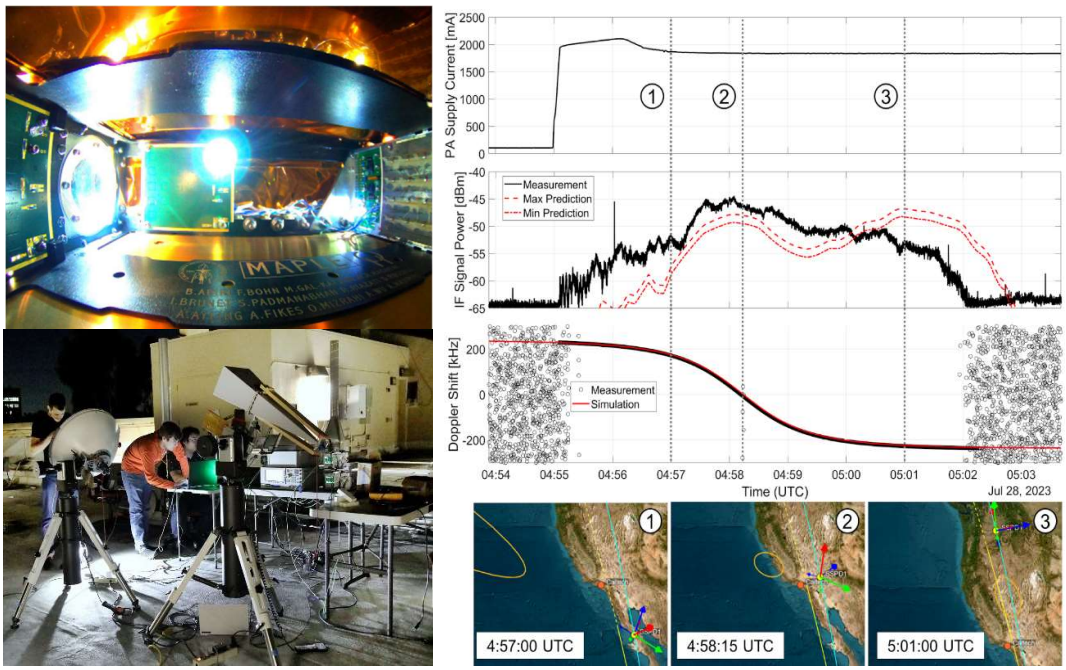

Figure 2.7. Interior of MAPLE (on top left), full ground station on the roof of Caltech's Moore Laboratory assembled before the experiment (on bottom left) and orbital tracking maps showing MAPLE during the pass (on the right) [13]

The second main space application is the power replenishment of space exploration vehicles. Generally solar power is chosen to fulfill the energy needs of space rovers. However, it becomes impractical when exploring the dark side of a planet. In order

to overcome this obstacle, methods of power beaming have been proposed for wirelessly charging the rovers by power beaming from a location on the same planet which has access to solar power more abundantly [32]. Also studies on powering spacecraft on dark areas during its mission via another satellite placed in an illuminated orbit have been conducted [33]. This will allow spacecraft and many rover missions planned on the Moon or Mars or any other planet to work continuously while establishing a greater efficiency than terrestrial power beaming applications due to the absence of atmospheric attenuation in space [34]. Current lunar or Mars rovers use Radioisotope Thermoelectric Generators (RTG) for meeting their energy needs. An illustration of some rover designs can be seen in Figure 2.8. However, due to the limited size of exploration rovers, RTGs cannot meet long-term energy needs of the rovers. Meanwhile, it results in additional cost and poses a safety risk to use rockets for supplying large amounts of radioisotopes. Therefore, usage of space power beaming systems to capture sunlight to convert it into electrical energy and transfer energy via a laser for wireless recharge of the rovers has great potential in Lunar or Martian environment.

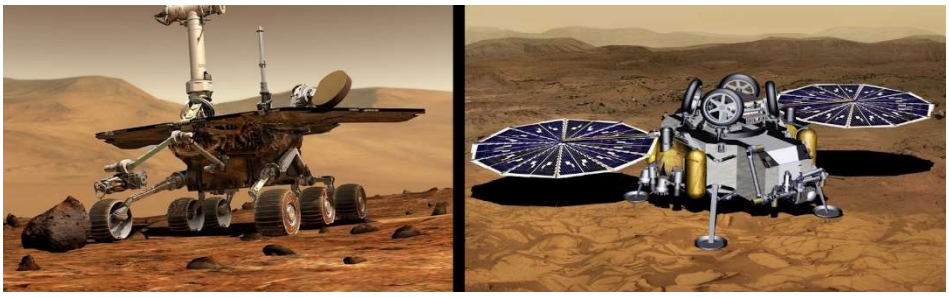

Figure 2.8. Two examples of Mars rovers and robots using solar energy for recharging [32]

2.1.4 Underwater Applications of Power Beaming

While space and aerial applications of laser power beaming are a greater focus of attention, it also has advantageous applications underwater. When used for communication purposes it is considered to exceed Gbps of data transfer with long transmission distances up to hundreds of meters [35-38]. The conventional methods using acoustic communication and radiofrequency consume high power, have high latency and causing incompatibility issues between high speed and long distance [39,40].

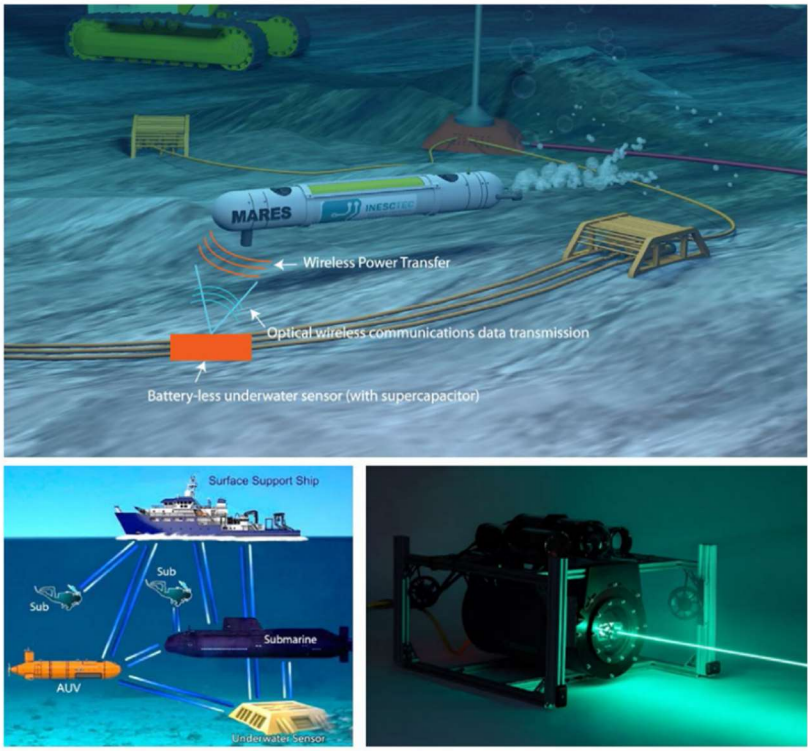

Figure 2.9. LPT for underwater applications [30]

There have been studies in 2019 [41], 2020 [42] and 2022 [43] using laser power beaming for underwater wireless optical communication (UWOC). These studies have used lasers around 450 nm wavelength for benefiting from the low attenuation of 450 nm to 550 nm wavelength light in water. Their main focus was communication purposes with 84 Mbps of data transfer rate being demonstrated. Illustrations of the concept are presented in Figure 2.9.

2.1.5 Daily Life Applications of Power Beaming

In addition to these outdoor and communication applications mentioned, power beaming can be used for many indoor and small-scale applications and obtain a place in daily life. For presenting what is possible, a few examples have been explained.

In 2017, researchers from the University of Washington have demonstrated charging a smartphone across a room with a 976 nm laser source [3]. The transmitter system could follow the phone in a room and automatically shutdown if anything passes the laser beam. The receiver included a photovoltaic cell placed on the back of a smartphone and a DC-DC converter for providing 5 V output to the smartphone. The system was able to deliver more than 2 W of power to charge a smartphone within 12 m distance. The setup can be viewed on Figure 2.10.

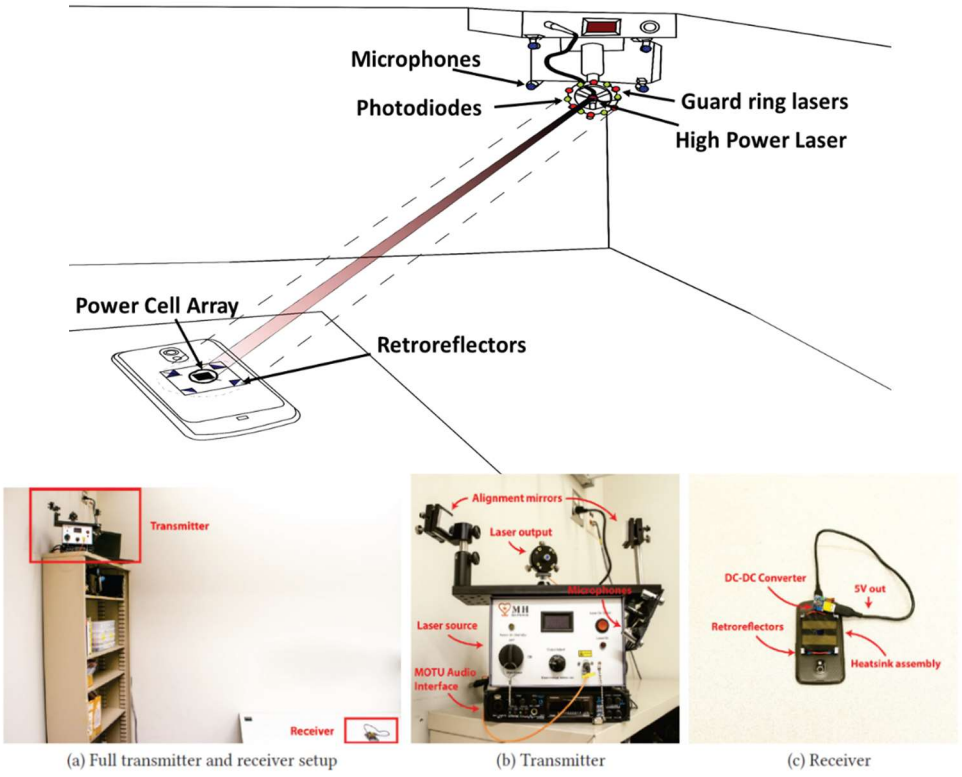

Figure 2.10. The illustration of phone charging with power beaming (on top), (a) the built setup, (b) transmitter and (c) receiver placed mounted on the back of a smartphone [3]

In 2020, researchers from Cornell University have produced microbots with microstructures on them, powered by the laser beam focused on them [44]. As can be seen from Figure 2.11, two photovoltaic cells are placed on the front and rear parts of the robot that are connected to actuators. When the beam is directed to one cell, the legs on that part move, and come back to their original position when the beam power is cut. Then the same is done for the cell that is connected to the other part. As a result of repeatedly powering back and front legs, continuous motion is obtained and the robot is both powered and controlled by power beaming.

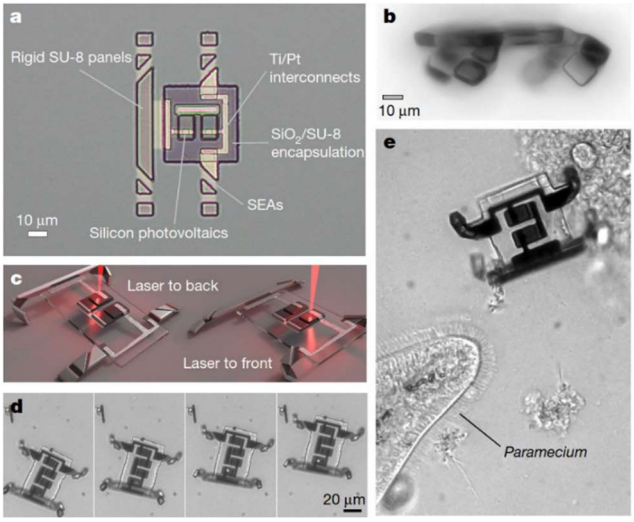

Figure 2.11. Microscopic robots powered and controlled by power beaming [44]

In 2024, researchers from Finland and Italy investigates fat tissue as a medium for communication in implantable/ingestible medical device (IMD) systems based on optical wireless communication (OWC) [6]. An illustration can be seen in Figure 2.12. The study uses 810 nm wavelength NIR light. The concept of harvesting power out of the signal that was used for communication has been demonstrated in a 2020 study [45]. So, by the usage of power beaming, the biomedical implants can be both communicated and charged without going through the costly surgical operations conventionally done for replacing the battery of implants.

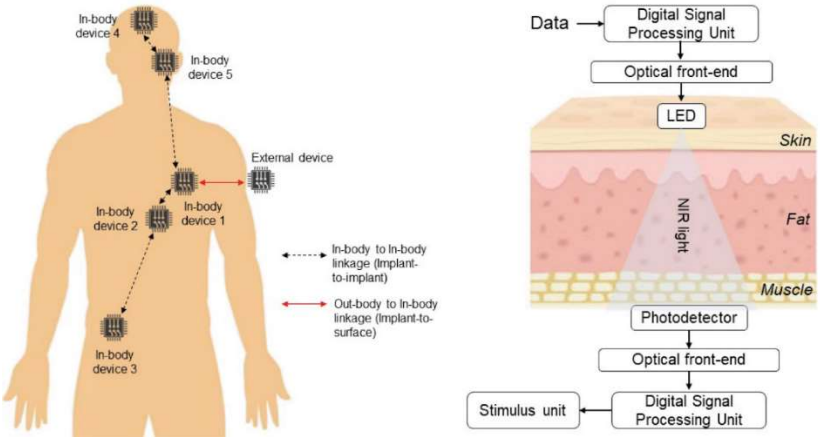

Figure 2.12. The diagram illustrating the generic architecture (on the left) and a close-up to the architecture in the study of using fat tissue as a communication medium (on the right) [6]

2.1.6 Laser Power Converters

Converting laser power to electricity by using a photovoltaic cell is a key element to laser power beaming. While being so, the same structure is also a key element for data transfer via optical fibers for communication lines or microsensors [46]. This structure is called as a laser power converter (LPC). There have been many LPC designs studied since 1981 [47]. Since these photovoltaic cell designs are purposed for communication, they are optimized for relatively low power laser beam. An LPC that can generate an output power of more than 5 W was not present until 2017. If the power is raised more than the optimized power, as will be explained in later chapters, the efficiency drops significantly. This makes them practically unusable for power beaming applications. However, together with the developing semiconductor industry and continued LPC studies, the provided power capacity also increased and may be combined with power beaming studies eventually.

Nevertheless, these studies are mostly focused on GaAs based materials and may provide a relatively high-cost alternative compared to silicon based photovoltaic cells.

In 2019, researchers from Fraunhofer ISE achieved 67.3% optical to electrical conversion efficiency from the 860 nm laser beam with intensity 9.6 W/cm² using a single-junction GaAs PV cell with a MgF2/Ag back mirror [48].

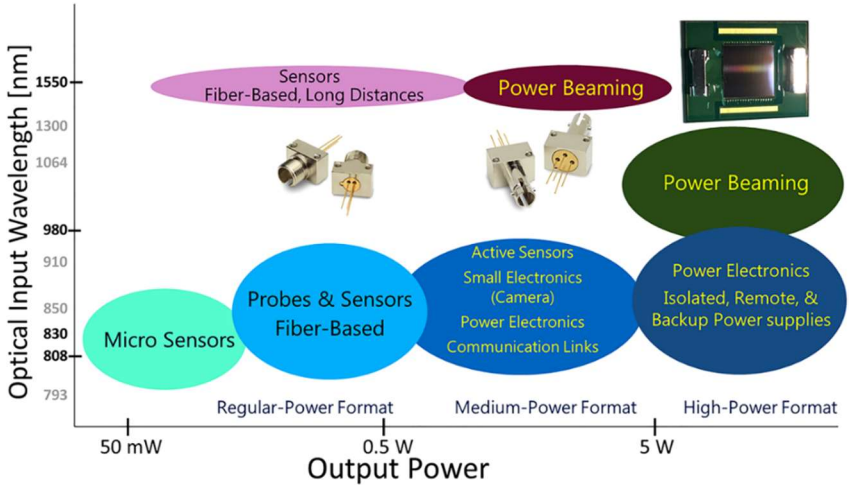

Figure 2.13. Illustration of the various OWPT applications organized according to the OPC's output power [46]

In 2021, researchers from the company Broadcom were able to achieve efficiency of more than 60% by using GaAs based materials and Vertical Epitaxial Heterostructure Architecture (VEHSA), generating 17.5 W of power from an 808 nm laser beam [46]. A graph that explains their products' application areas is seen in Figure 2.13. In the same study, they also obtained 48.9% efficiency when generating 22 W of power from a 980 nm laser beam.

2.2 Contributions of This Study

In this work, the effects of 1030 nm to 1080 nm laser light on different types of silicon photovoltaic cells (monofacial PERC, bifacial PERC and IBC) under varying intensities have been investigated. This was established by fabricating a wavelength tunable laser. It can be tuned to provide different wavelengths of light ranging from 1030 nm to 1080 nm. It is a high-power fiber laser capable of providing more than 50W of power. In addition, wire grid optimization of mono-facial and bifacial PERC

cells was done with the simulation program Griddler 2.5 PRO. These wire grid-optimized cells were fabricated and experimented with under laser illumination.

A custom electronic measurement system was built for characterization of the cells. It is working by iterated measurements of the current and voltage generated by the PV cells while varying the load electronically and plotting the IV curve of the cell. Long-range outdoor measurements were conducted at approximately 100 m distance with an IBC cell and the novel design of thin multi-cells with bifacial PERC cells were studied.

To the best of our knowledge, a wavelength tunable laser or the IBC structure was not present in any other power beaming study except for this one.

CHAPTER 3

THEORY OF POWER BEAMING

Power beaming concept basically covers transferring energy wirelessly via electromagnetic radiation with a transmitter, and receiving it with a receiver. An updated formal definition is “Uncoupled wireless power transfer in which the link distance exceeds the sum of the largest dimensions of the transmit and receive structures, and where at least 1% end-to-end energy transmission efficiency is obtained.” [49]. In this study, the choice of transmitter has been a wavelength tunable infrared laser, and for the receiver, silicon photovoltaic cells have been chosen.

Silicon, as a material for photovoltaic applications, offers several advantages. It has high efficiency due to its bandgap energy matching with infrared photon energy [50]. Additionally, silicon's economic feasibility is primarily driven by its abundant availability and its widespread use in solar applications. As one of the most common elements on Earth, silicon is readily accessible, making it a cost-effective choice for various industries. Its role in the production of photovoltaic cells for solar panels is particularly significant in renewable energy markets, reinforcing its economic viability, reducing costs through the big scale production facilities. Consequently, silicon continues to be a cornerstone material in advancing sustainable energy solutions while remaining economically attractive.

Apart from economic aspects, the physical properties of silicon is also fitting power beaming applications well. Its ability to withstand high photon flux levels without significant degradation ensures reliable operation even under intense conditions. [51]

As the transmitter, the choice of an infrared fiber laser reciprocates the economical and physical advantages of a silicon photovoltaic receiver. In addition to bandgap matching of IR with silicon, fiber lasers have become economically feasible over the years and offers a robust way of obtaining IR well-collimated beam.

3.1 Fiber Lasers

On the transmitter side, monochromatic infrared light is being generated by a tunable wavelength high-power CW laser.

The operation principle of a laser consists of two parts; stimulated emission inside a gain medium (an amplifying medium), and optical feedback to feed the light back into the amplifier for continued growth of the developing beam [52]. This is established in the oscillator cavity of the laser. Later, the obtained signal is amplified in the amplifiers and collimated by a focusing lens.

After obtaining a signal from the oscillator, this becomes the seed for the amplifier. In the amplifiers, pump light of 915 nm or 975 nm light is converted to the wavelength of the seed, resulting in an increased power at the resultant signal, establishing stimulated emission.

The pump light is pumped to the cladding of the double-clad gain fiber. The structure of the gain fiber is designed so that Yb atoms absorb the pump light and amplify the signal propagating in the fiber core. For this purpose, the core silica is doped with Yb atoms and covered by the first cladding. It is then covered with a polymer of refractive index lower than silica which makes up the second cladding. The refractive index of non-doped silica is less than the Yb-doped silica as well. Thus, the light propagating in the core is subject to total internal reflection as it is incident to the core-cladding interface and thus continue propagating. Similarly, the pump light in the cladding propagates within the first cladding with total internal reflection (when it is incident on the second cladding), or, gets absorbed (when it is incident on the Yb atoms present) at the core part of the fiber. The structure of a double-clad fiber is seen in Figure 3.1.

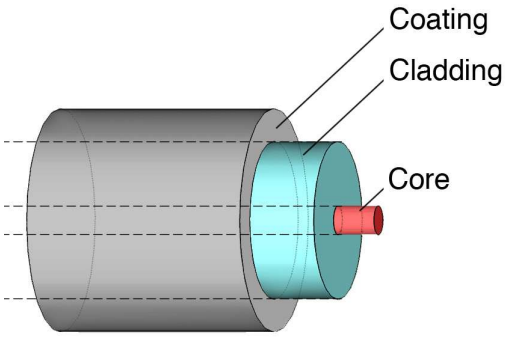

Figure 3.1. Double-clad fiber illustration showing its structure [53]

The electrons which are excited by the absorbed pump light interacts with the optical feedback and provide stimulated emission. The optical feedback is provided in the cavity of the oscillator with a portion of the light that is circulating within. The circulating light becomes the signal and amplified with stimulated emission.

The resultant optical output is highly directional, coherent, monochromatic light that will be used to transfer optical power from the transmitter to the receiver.

3.2 Photovoltaic Cells

On the receiver side, light is converted into electricity via a silicon photovoltaic cell. A photovoltaic cell works with the photovoltaic effect, which is defined as “the generation of a potential difference at the junction of two different materials in response to electromagnetic radiation” [54]. It is made up of three parts; generation of charge carriers due to the absorption of photons at the junction, separation of the charge carriers, and, collection of the charge carriers at the terminals of the junction.

In an ideal semiconductor, electrons can only be present below the energy levels of valence band edge and above the energy levels of conduction band edge. The energy difference between these two levels is called the bandgap. Thus, in an ideal semiconductor, if a photon is absorbed by the material, photon’s energy must be

greater than the bandgap, otherwise it is not absorbed and continues propagating without interacting with the material.

In a real semiconductor, the energy change of the electron depends on the k-vector describing the momentum of the electron. If the energy bands are flat and the electron can change its energy with no momentum change, then it is called a direct bandgap material. If the energy bands are not flat and the electron needs an exchange of momentum with the crystal lattice for changing its energy level, then it is called an indirect bandgap material. The illustration of this phenomenon is seen in Figure 3.2 [54]. Silicon, being the material of PV cells used in this thesis, is an indirect bandgap material. Due to this, the absorption is lower with respect to a direct bandgap material. However, the low cost, abundancy and the wide usage of silicon in the industry still makes it a feasible choice.

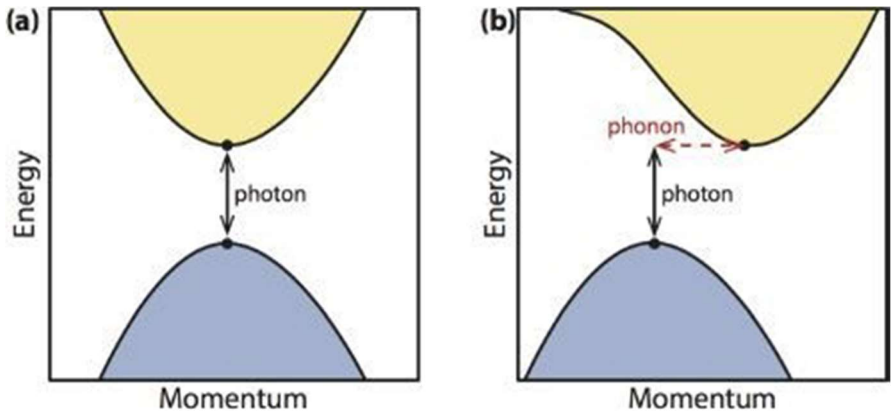

Figure 3.2. The dispersion diagram of (a) a direct bandgap semiconductor and (b) an indirect bandgap semiconductor [54]

After an electron absorbs a photon and reaches the conduction band, there is a void space left in the valence band. That void space is named as a “hole” and it behaves as if there is a positive charge in that void. So, the charge carriers are generated due to the absorption of a photon and excitation of an electron. These charge careers (excited electrons and holes) as a pair are called an electron-hole (e-h) pair.

If this e-h pair is not subjugated to any collection or separation, then the excited electron at the conduction band falls back to the valence band, resulting in a

recombination. The recombination can be radiative or non-radiative. Radiative combinations result in a new photon creation and the non-radiative ones result in an energy transfer to other holes or electrons, or to the lattice vibrations. Illustration can be found in Figure 3.3 [54].

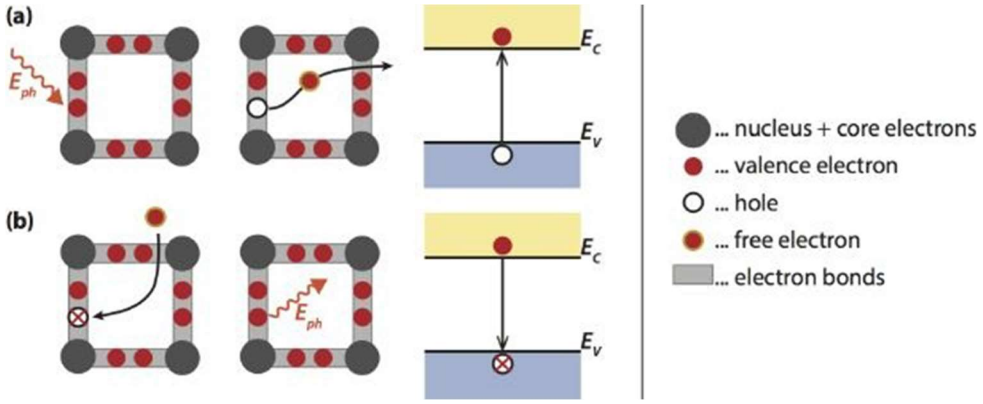

Figure 3.3. Visualization of bandgap-to-bandgap (a) generation; and (b) recombination processes using the bonding model and the energy band diagram [54]

In order to extract the energy of an e-h pair and perform work in an external circuit, there needs to be a "semipermeable membrane" where the electrons move in one direction and holes in the other direction [55]. For that purpose, a p-n junction is formed.

A p-n junction is established when an n-type material (one that has excess of electrons) is joined with a p-type material (one that has excess holes). Then the excess electrons in n-type material diffuse into the p-type material and similarly excess holes in p-type material diffuse into the n-type material. The gradual depletion of the charge carriers results in a space charge formation. This is duo to the ionized donor and acceptor atoms which is not compensated by the mobile charges. It causes an electric field at the region between the two materials, also called as "space charge region". This way, the charge carriers are separated in a photovoltaic cell with the force due to electric field. This implies that the radiative energy that incident photon had was transformed into the chemical energy of the e-h pair after absorption, and

can be transformed to electrical energy by driving an external circuit before recombining. As the charge carriers are collected at the terminals of the junction the energy is harvested from the system. However, there are multiple mechanisms in which the energy is lost.

3.3 Loss Mechanisms

The two most important ones are, inability to absorb photons that have energy less than the bandgap energy and thermalization of the photons that has greater energy than the bandgap (the excess energy more than the required excitation energy/bandgap energy is turned into heat). In solar applications, these two make up approximately half of the total loss for converting solar energy into electrical energy [56].

Initially at the absorption stage, if the incident photon does not have enough energy to excite an electron, it won't be interacting with the material and get transmitted. So, this transmitted light will be basically lost and decrease the efficiency.

After the absorption stage, not all the absorbed energy is transferred to carrier generation stage. The excess energy of a photon, after subtracting the bandgap energy from the photon energy, is transformed into heat and cannot be converted to electrical energy.

So, for the highest efficiency of energy conversion, wavelength of the incident light must be chosen so that the photon energy is matching the bandgap energy of the receiver material (silicon within the scope of this study). Any difference between the energies will result in a loss either as heat production or light transmission.

The bandgap energy of silicon is 1.12 eV at 300 K which require 1107 nm or smaller wavelength light to excite an electron, however, the bandgap energy has a dependency on temperature [57]. As the temperature decreases, the bandgap energy increases thus the wavelength must be smaller in order to be absorbed.

However, when high power laser beam is incident on a cell, there occurs a heat buildup and temperature fluctuations. Thus, the highest efficiency for a specific design might not be the one with highest absorption. A lower absorption that enables better temperature control may result in a better overall efficiency. Hence, it is a matter of investigation to determine which wavelength near the bandgap results in better efficiency at higher powers.

The loss mechanisms that occur in higher and lower powers can be listed as; direct recombination, Shockley-Read-Hall recombination, Auger recombination and surface recombination. This is basically the recombination of e-h pairs before getting collected and utilized by an electrical load.

Direct recombination occurs as the e-h pair comes to the end of its lifetime and recombines by a transition from the conduction band to the valence band directly.

Shockley-Read-Hall (SRH) recombination is facilitated by an impurity atom or lattice defects and the energy is lost as heat rather than radiative recombination. It is illustrated on Figure 3.4.

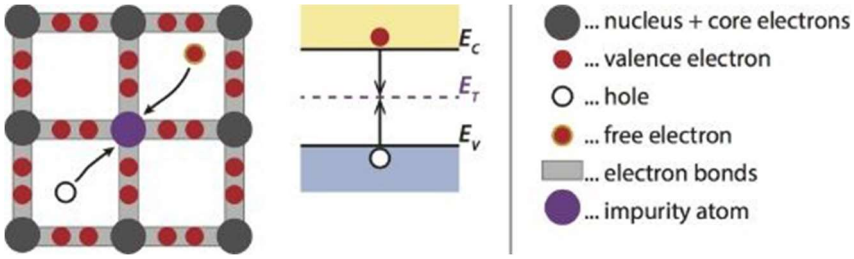

Figure 3.4. Visualization of Shockley–Read–Hall recombination using the bonding model and the energy band diagram [54]

In indirect bandgap materials Auger recombination becomes important (illustrated on Figure 3.5). It can either happen by an excited electron giving its energy to another excited electron, sending it to higher energy levels of the electronic band, or, a hole, giving its energy to another hole, sending it to deeper levels of the valence band. Both of the energized particles result in relaxation and transferring that extra energy to vibrational energy of the lattice or phonon modes, at the end, lost as heat in the

system. Auger recombination becomes more important as the doping level increases for a photovoltaic cell for high intensity light applications.

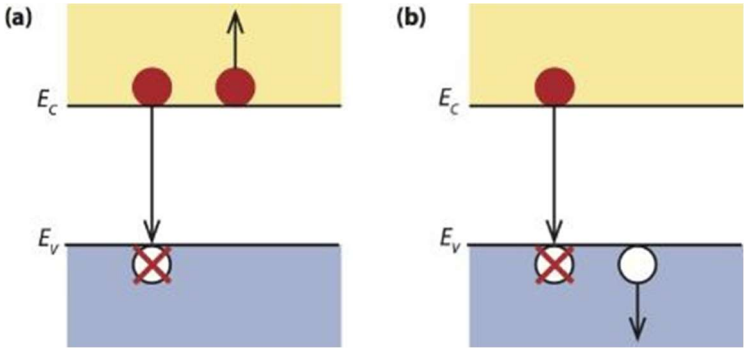

Figure 3.5. Illustration of Auger recombination with (a) two electrons; and (b) two holes involved. [54]

Surface recombination occurs due to the electrons on the surface of the semiconductor that does not have a partner for having covalent bond with. Due to this, the non-bonded potential covalent bonds, or the "dangling bonds" provide trap states in the bandgap. These trap states provide a suitable condition for SRH recombination. However, surface recombination is not dominant unless the semiconductor is very pure.

3.4 Thermodynamical Efficiency Limit

Thermodynamical limits of photovoltaic conversion, when multicolor light of sun is converted, has the limit of 31.0% efficiency [58] with one junction and natural sunlight. Values for varying number of junctions and solar intensities are presented on Table 3.1. This is called the Shockley-Quisser limit and this value is calculated for 1.34 eV light (925 nm) incident with 1 sun (1 kW/m^2) intensity.

Table 3.1 Multicolor solar energy conversion efficiency [58]

C	*n*	*Photothermal*	*Photovoltaic*
1	1	53.6	31.0
	2	60.9	42.9
	3	63.3	49.3
	…		
	∞	68.2	68.2
100	1	67.0	35.2
	2	71.7	48.4
	3	73.2	55.6
	…		
	∞	76.2	76.2
46300	1	85.4	40.8
	2	86.1	55.7
	3	86.3	63.9
	…		
	∞	86.8	86.8

“n” is the number of layers stacked (the number of junctions), and “C” is the concentration of light with respect to natural sunlight. When both the limit of n goes to infinity and maximal realizable light concentration from sun (multicolor) is considered in Earth’s environment, the upper limit of any solar energy conversion efficiency thermodynamically possible is 86.8% at maximal sun intensity and

infinite junctions. Both photovoltaic and photothermal limits approach the same value.

In addition, in a study in 2013 [59] it was emphasized that the Shockley-Quisser limit assumes that the only recombination mechanism is direct recombination. However, silicon being an indirect bandgap material makes Auger recombination to be dominant. The theoretical efficiency would decrease even more as the light intensity increases due to increasing Auger recombination with higher intensity. Also, note that Shockley-Quisser Limit does not take into account the optical losses and the collection losses.

However, a critical point to be emphasized is that, this is not the case for monochromatic light used in non-solar photovoltaic applications. It was presented in the 2001 study by Martin Green [17] that, in principle, photovoltaic cells can obtain efficiencies arbitrarily close to 100%. This depends on the intensity of light, its wavelength, and the range of angles at which the cell emits or absorbs light. The illustration of the study on an IV curve is seen on Figure 3.6.

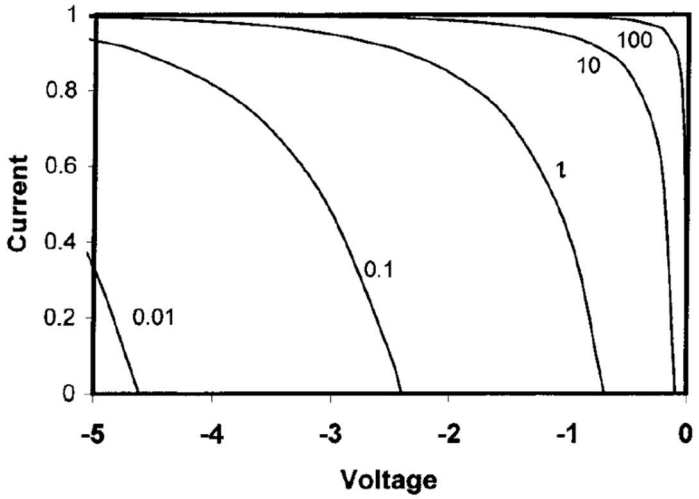

Figure 3.6. Calculated normalized current-voltage curves for an idealized solar cell for increasing normalized monochromatic light intensity, i. The voltage is expressed in units of kT/q below E/q, the potential corresponding to the photon energy, E [17]

Thus, by matching the laser wavelength and the bandgap energy of silicon, and, establishing light management in a design, maximizing the absorption of incident light, also, optimizing the design for the desired intensity of light and carrier collection at metal contacts, it is possible to reach efficiencies close to 100%.

3.5 Advantages of Different Wavelengths for Power Beaming

It is possible to establish power beaming by using a great variety of wavelengths, however, some wavelength regimes have much more outstanding advantages than others, thus the studies related to power beaming have been mostly focused on systems using transmitters producing these wavelengths of light with their receivers optimized to it. The most common wavelengths studied or long-distance power beaming are microwave and near-infrared regime while terahertz regime also being investigated [61]. The main advantage of these three regimes is that there is an atmospheric window in each of these regimes, while also being possible to feasibly establish a transmitter source and a receiver specifically designed for that wavelength. An atmospheric window is a wavelength regime that can propagate through the atmosphere without getting absorbed by the materials present in the atmosphere [62]. While the atmospheric window is a common advantage in all three, their benefits are different concerning three aspects; distance between transmitter and receiver, the size of the receiver, and the weather conditions.

Over relatively long distances, diffraction of the beam is limiting the usage of a wavelength. The approximate range is calculated by the Rayleigh range which is 2.8 m for microwave (2.46 GHz), 340 m for terahertz (300 GHz), and 228 km for infrared (1500 nm) [61], a range of 9800 km was also reported for infrared (1060 nm) in another study [63]. Thus, for longer distances infrared is much more advantageous regarding its ability to keep a well-collimated beam without spreading due to diffraction. Using microwaves over longer distances would require the power of the transmitter to be much larger and spread over a large area, causing a safety hazard in that area. It also necessitates the receiver to be impractically large for

carrying on air vehicles while IR photovoltaic receivers can be made as small as a single solar cell size. So, it is not feasible to transfer energy with microwaves for aerial or space applications, but they are fitting short distance applications. For example, powering devices in a room would be feasible with microwaves, and the required hardware would be much more economical for the lower power needs of household items when compared to an infrared laser and a photovoltaic array. Terahertz on the other hand, has advantages in foggy and dusty air. When the size of the particles in air are between 1 μm to 50 μm, scattering and attenuation are weaker for terahertz waves with respect to infrared. Infrared power beaming is not possible in foggy weathers and dust while terahertz is still possible for the 100m range. These properties are promising for aerial applications, however, more research needs to be done in terahertz power beaming regarding the choice specific wavelength for the specific application area and for increasing the efficiency of receivers. It is possible to find terahertz receivers with ~2% efficiency at most for 303 GHz while at the same time ~40% efficiency is possible for 94 GHz electromagnetic waves.

Considering the present efficiencies of photovoltaic receivers optimized for infrared (more than 65%), infrared beam's well-collimation properties, its receivers' relatively small size and the present technological readiness level for IR transmitter and receiver (high-power IR semiconductor lasers and silicon photovoltaic cells), infrared regime is the most feasible wavelength regime for long range energy transmission.

However, with all these promising advantages, there are two main obstacles for power beaming; the efficiency of harvesting the light that has very high intensity on the receiver and the relatively low efficiency of light generation on transmitter.

If the history of the development of lasers in different wavelengths is inspected, it is seen that it was not possible to fabricate a high-power laser with feasible efficiencies until the last decades.

In 1995, it was only possible to obtain 25% electrical to optical conversion efficiency in a laser producing 980 nm wavelength light while only delivering 1.2 mW [64]. In

1996, this was raised to 27% efficiency providing 2.7 mW of light [65]. In 1998, a 532 nm laser was able to provide 20 W optical power at efficiency of 14.2% [66]. For the range 780 nm to 1100 nm, the lasers that could provide more than 10 W of optical power was in 2006 [67]. This is the regime where there is an atmospheric window present. The laser that was fabricated in 2006 was operating at 1060 nm and generating 11 W optical power with the efficiency of 44%. Then the development continued with a similar pace to solar industry development as mentioned in previous sections; in 2008 3500 W laser at 980 nm with 51% efficiency [68], in 2012, 99.6 W laser at 1028 nm with efficiency 45% [69], in 2013, 200 W 940 nm with 53% efficiency [70]. Then in 2018, 52.4% efficiency in 885 nm providing 2.1 W [71], 38.8% efficiency in 912 nm providing 6.9 W [72], 21% efficiency in 1060 nm providing 6.9 W [73] were established. In 2022, it is possible to find a 915 nm laser with 72.6% efficiency while providing 15.3 W power [74].

It can be observed that the electrical to optical conversion efficiencies of lasers (especially semiconductor lasers) have been improving in the same decades where optical to electrical conversion efficiencies of photovoltaic cells have been improving. Both of these advancements being dependent on the growing semiconductor technology.

As the lasers getting more and more efficient, robust and economic, there was still the obstacle of harvesting that laser power on the receiver side. It is a fact that higher efficiency solar cells were developed and photovoltaic technology was improving, however, these studies were mainly focused on harvesting sunlight, which contains multi-color light and having an intensity no more than 1 kW/m^2. In laser power beaming, for practical terrestrial applications, due to the necessity of small aperture size the beam intensity is very high, implying many kilowatts per meter square and the effect of each wavelength is different in terms of absorption and electron hole pair creation.

CHAPTER 4

IMPLEMENTATION OF IR LASER AND SI PV CELLS

In order to find the optimal system parameters for power beaming, both the transmitter and the receiver has to be investigated.

In the transmitter side, a tunable wavelength (1030 nm – 1080 nm), matching the bandgap energy of silicon, high-power CW fiber laser system was developed and integrated into a long-range collimation and beam direction controlling system. The laser developed for this study is capable of providing more than 50 W of optical power. Experiments with different wavelength and intensity of light was made to find out which wavelength has the highest absorbance when incident on silicon.

On the receiver side, computer aided simulations were completed for wire grid optimization of the busbar and fingers of a PERC photovoltaic cell within the scope of this project. New PERC cells were fabricated according to the simulation results and studied under laser light. A novel design has been introduced which is composed of multiple thin bifacial PERC cells positioned perpendicular to the axis of light propagation. This design was studied with series and parallel connections under varying wavelength and intensity. In addition to monofacial and bifacial PERC cells, commercial IBC cells were also studied under laser light. Later, a panel made with multiple thin bifacial PERC cells and an IBC cell were experimented in outdoor environment with a longer distance.

4.1 Fabrication of the Wavelength-tunable High-power CW Fiber Laser

On the transmitter side, monochromatic infrared light is being generated by light amplification by stimulated emission of radiation. The laser system consists of an Oscillator, Pre-Amplifier (First Amplifier), Final Amplifier (Second Amplifier), and

a 3D motorized stage. The gain medium for the laser is an Yb doped gain fiber, in which the Yb atoms' electrons are excited by the pump light of 976 nm (in 1st and 2nd pump diodes) or 915 nm (in 3rd pump diode) propagating in the cladding of the gain fiber. Due to the high absorption rate of Yb near 976 nm [75], the pump diodes are chosen near that wavelength. The absorption and emission rate for varying wavelength can be seen in Figure 4.1. The excited electrons have a meta-stable state which makes stimulated emission at the tuned wavelength propagating in the core of the gain fiber.

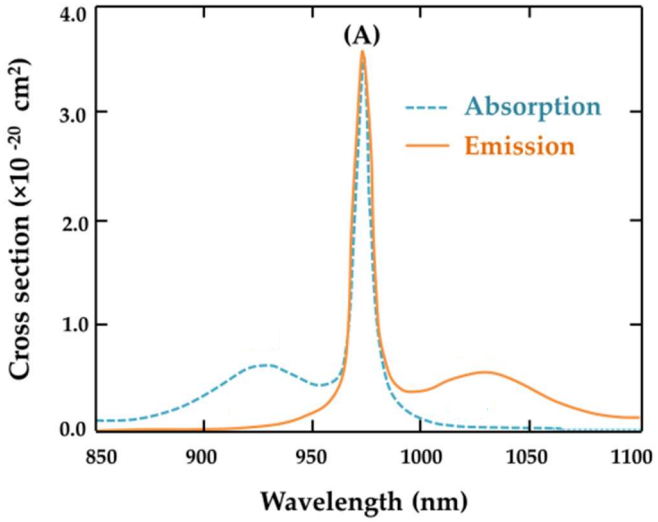

Figure 4.1. Absorption and Emission spectrum of Yb [75].

The schematic of the laser system can be seen in Figure 4.2. The oscillator provides a cavity where the laser signal can be generated. Pump Diode 1 is a multi-mode pump laser diode stabilized at 976 nm capable of providing 9 W. The pump power enters the cavity via multi-pump combiner 1 (MPC1), continues to propagate through 1.2 m of Yb-doped double clad gain fiber with core to cladding ratio 6/125 microns. Isolator 1 located after the oscillator gain fiber is rated for 2 W and protects the system from any possible back reflection and provides unidirectional light propagation inside the cavity. The power then reaches Collimator 2, continue propagating in free space, gets diffracted at the filter and enter Collimator 1. The

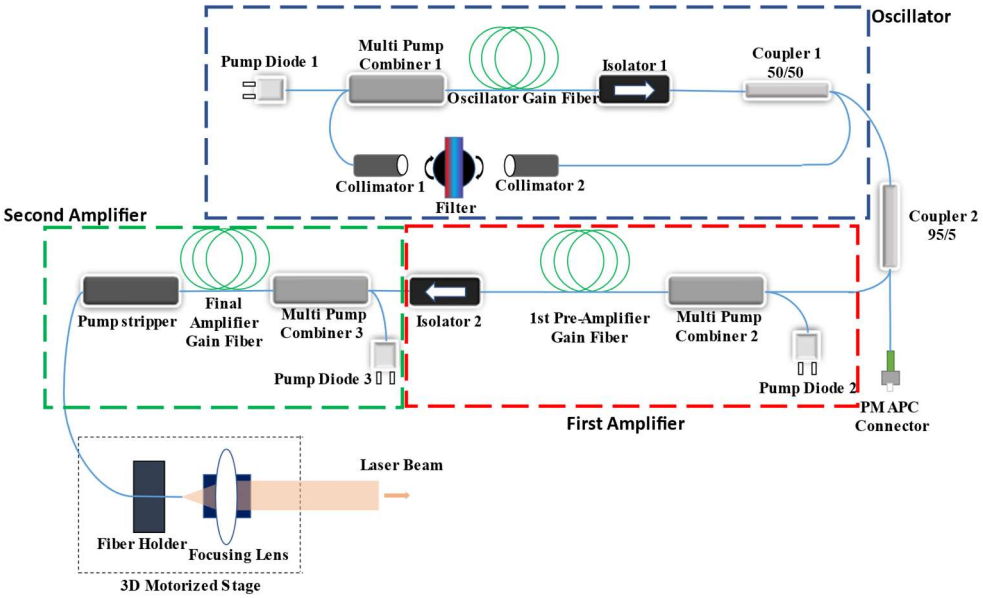

Figure 4.2. Schematic of the high-power CW tunable wavelength laser system developed in this study, the diffracted light inside the Oscillator is coupled into the collimator and the tuned wavelength obtained from it is amplified in the First and Second Amplifiers

filter is made up of a transmission grating with 800 lines per mm (lpmm) fixed on a Thorlabs rotating stage. The 976 nm light that is absorbed by the Yb atoms in gain fiber results in an emission in 1000-1100 nm wavelength. The emitted light in this range is diffracted at the filter, and by rotating the grating, the desired specific wavelength is coupled to the Collimator 1. As this chosen wavelength propagates in the core of the gain fiber, the emission of Yb atoms is stimulated to emit the same wavelength in the core, thus light amplification by stimulated emission is established. Half of the power for the next amplifiers is exiting the oscillator via Coupler 1 and the other half continues circulating inside the cavity. The suggested maximum power by the manufacturer is approximately 1 W for the collimators and Coupler 1. Due to this limitation, 1.3 W of pump power was not exceeded for the oscillator for operation, obtaining approximately 100 mW of signal from the oscillator. This can be increased if appropriate components for higher powers are installed. The oscillator power output with respect to the pump power from Pump Diode 1 can be observed in Figure 4.3.

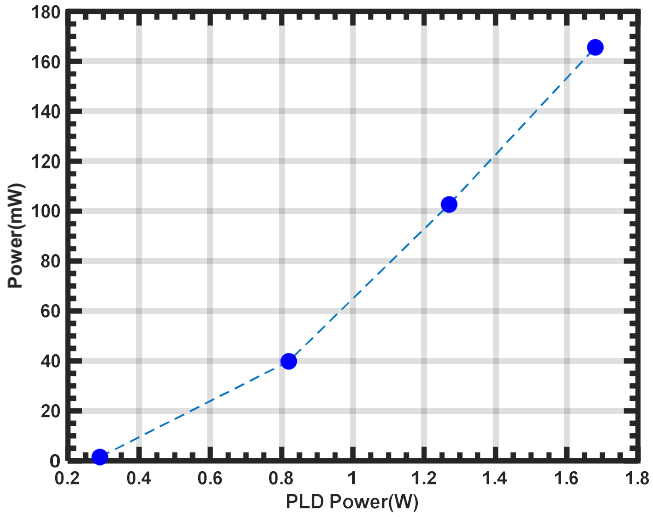

Figure 4.3. Output power of the oscillator with respect to pump power from Pump Diode 1 measured at 1027 nm

The power output for different wavelengths is different. The output power with respect to wavelength is plotted on Figure 4.4 (a) where the PLD power is fixed to 1.3 W for all wavelengths. Throughout the rest of the measurements in the related part, it will also be kept at 1.3 W. Figure 4.4 (b) demonstrates typical spectrum of the oscillator recorded near the wavelength 1060 nm. The full width at half maximum (FWHM) for a typical spectrum is 0.1 nm.

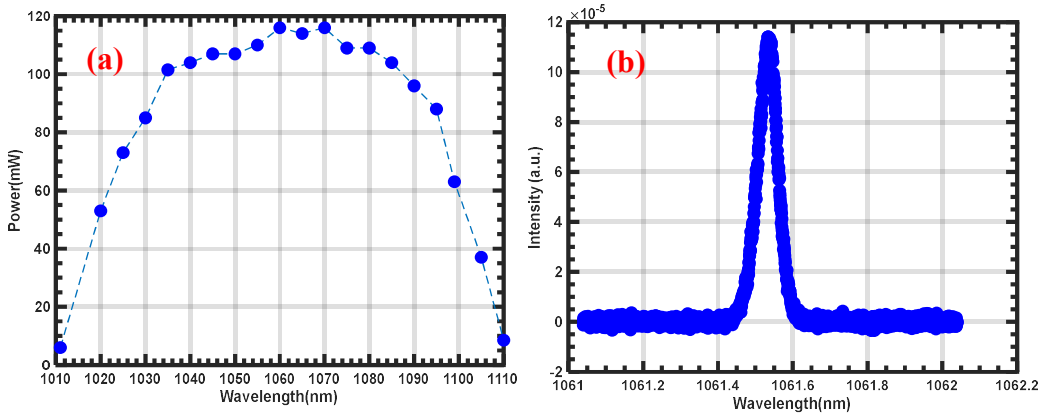

Figure 4.4. (a) Output power of the oscillator with respect to the tuned wavelength, (b) typical spectrum recorded at 1061 nm

The wavelength-tuned light exiting the oscillator and reaching the first amplifier for power amplification has forward pumping established. The pumped light passes through 5 m of Yb1200 6/125 DC gain fiber which is fixed on an aluminum plate that prevents heat buildup (Figure 4.5 (a,1)). The pump diode used in this amplifier (Pump Diode 2) is an MM pump diode which is wavelength stabilized at 976 nm, capable of providing 18 W of power. However, to avoid damaging the gain fiber, the pump power was not increased more than 5 W during normal operation of the laser. The maximum power output that was measured is 6.3 W (at 1060 nm) with 14 W of pump power from this stage. Figure 4.6 (a) provides the dependency of output power from the first amplifier vs pump power at the wavelength of 1060 nm. All of the wavelengths that are tunable in the oscillator reach nearly the same power level when the same amount of pump power is provided, this can be observed in Figure 4.6 (b).

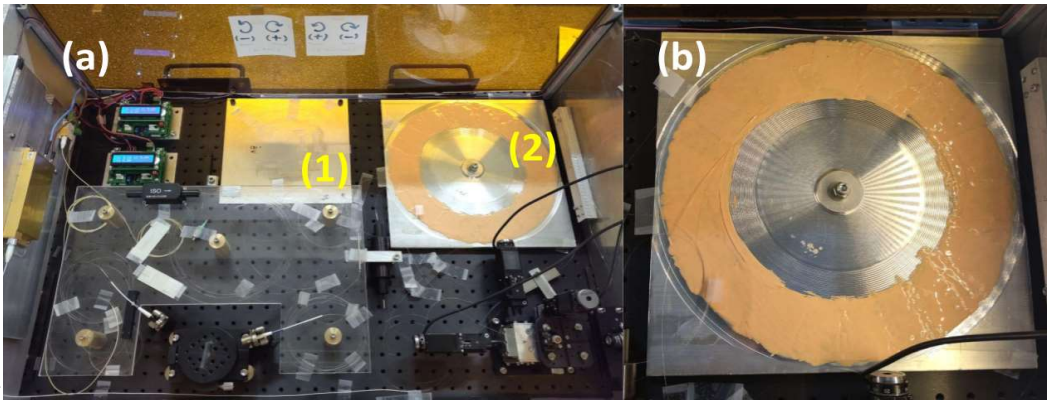

Figure 4.5. (a) Gain fibers of first amplifier (1) and second amplifier (2) on the aluminum plates, (b) Close-up on the second amplifier gain fiber

The output of the first amplifier exits via Isolator 2 and continues to the final amplifier. The final amplifier is based on 18 m of double-clad Yb-dopped fiber (Yb1200-14/250 DC), which is forward pumped via MPC 3 (Figure 4.1). The pump diode in this stage (Pump Diode 3) is an MM pump diode at 915 nm which can provide more than 100 W. At the output, 50 W of power has been measured while pumping approximately 75 W of pump power from Pump Diode 3. This implies that

the efficiency is approximately 70% in the second amplifier. The dependency of the output power of the second amplifier on pump power is shown on Figure 4.7.

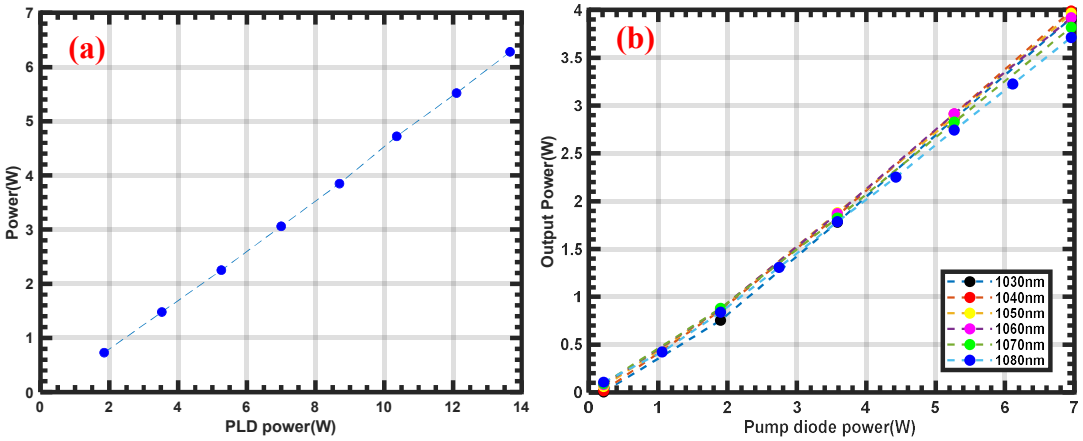

Figure 4.6. (a) Output power at 1060 nm after first amplifier with respect to pump power from Pump Diode 2 and (b) power output when wavelength is tuned to different values

The gain fiber of the second amplifier has been placed in a special plate for cooling (Figure 4.5 (a,2),(b)). There are grooves opened on the plate's surface so that the fiber fits inside well, both fixing its position and providing efficient cooling of the fiber. The fiber is covered with high thermal conductivity thermal glue for better cooling. In a system with efficient cooling, it is possible to go even higher powers without burning the gain fiber which, is one of the most critical points of a high-power fiber laser.

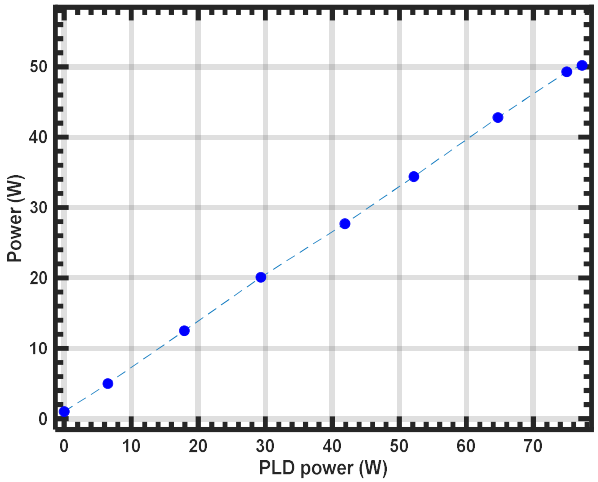

Figure 4.7. Dependency of the output power of the second amplifier on pump power

Finally, the output from the final amplifier exits the fiber at the 3D motorized stage that is capable of 2 mm motion in XYZ directions with 0.2 µm resolution. It has a focusing objective with 10X magnification. The tip of the fiber here has been cleaved at 8 degrees to prevent back reflection. By using the motorized stage, it is possible to adjust the beam diameter. The laser system is suitable for mobile use with a UPS and movable cart. The visual of the laser system is shown in Figure 4.8.

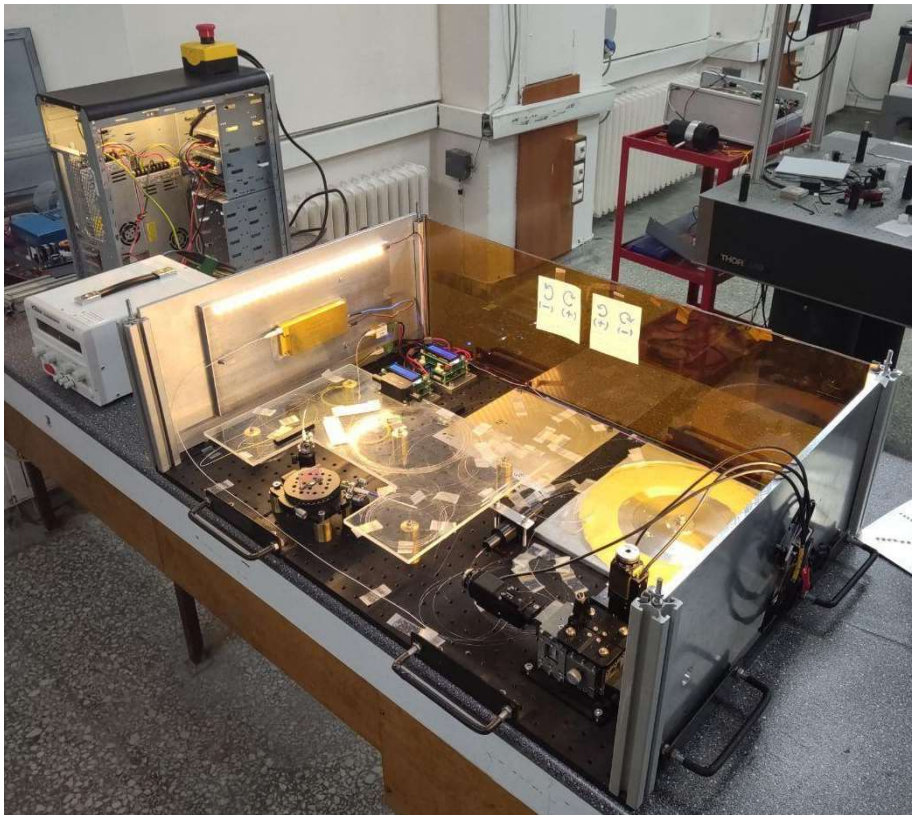

Figure 4.8. The overview of the laser system with power supplies gathered in the metal casing illuminated on the left section and all the optical components located on the optical breadboard located on the right section of the image

4.2 The Simulations for the Receiver PV Cells

On the receiver side, as mentioned in Chapter 3, there are two main obstacles for energy conversion; the inability of complete light absorption, and the inability of

collecting all the generated carriers. In order to collect the generated carriers more efficiently, computer aided simulations were done for wire grid spacing of the busbar and fingers for both monofacial and bifacial PERC photovoltaic cell structures. New PERC cells were fabricated according to the simulation results and studied under laser illumination.

The simulation software, Griddler Pro 2.5 was used for the design and simulation. This software simulates the IV characteristics of the solar cell and calculates the parameters like efficiency at MPP, open circuit voltage (V_{oc}), and short circuit current (I_{sc}). The simulations have been done for p-type c-Si wafer with Boron dopant with 1.3 ohm-cm resistance. Since Griddler is developed for solar research primarily, monochromatic laser light was defined as a custom illumination source in the software. Optical spectrum of the laser was recorded with an Optical Spectrum Analyzer (OSA) and then its scale was adjusted so that the integral of gaussian beam is equal to the power of the beam measured by optical powermeter. A beam of 1060 nm and 1 kW/m^2 intensity was introduced to the simulation.

Using the simulation, a sweep for different values of pitch (center to center distance) of the fingers and finger width was done to find the ideal wire grid spacing. It can be seen from Figure 4.9 that the ideal wire grid spacing for monochromatic laser light is not the same with solar light (AM1.5g).

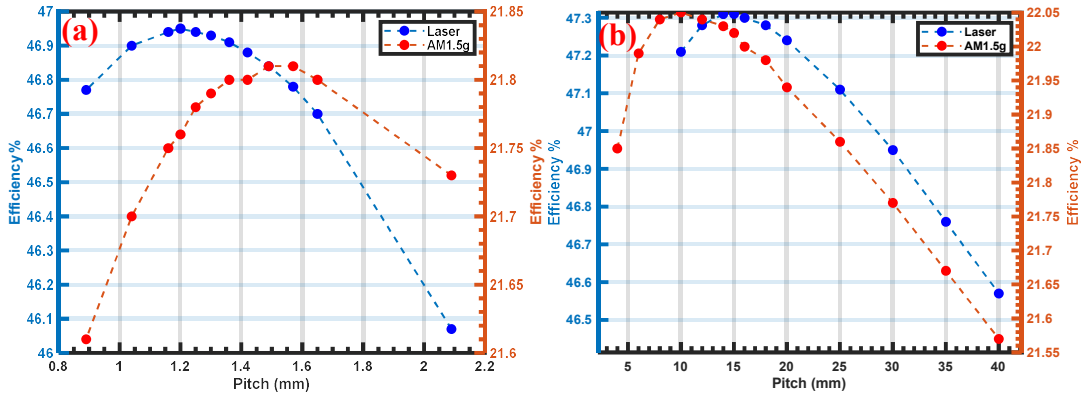

Figure 4.9. (a) Efficiency versus pitch (center to center distance) of the fingers and (b) efficiency versus finger width, both for solar spectrum and laser spectrum

The simulation results indicate that the efficiency of the wire grid optimized cell for laser light would have 21.81% efficiency under AM1.5g (normal sun spectrum and 1 kW/m^2 intensity), and with the laser source of 1060 nm it would reach 46.95% efficiency under 1 kW/m^2. This monochromatic efficiency is very high when compared to the normal sun spectrum, however, as it was mentioned in Chapter 3, it is possible to obtain efficiencies arbitrarily close to 100% when monochromatic light is used, so the simulation results are actually in accord with the theoretical expectations while being much lower than the theoretical maximum efficiency. However, for efficiencies closer to 100%, the wafer thickness of a single junction PV cell needs to be much greater than the standard solar cell thickness (~3000 μm ideally [76]).

4.3 Thin Multi Cell Design

A novel design has been introduced for increasing the efficiency of the receiver module. It consists of multiple thin bifacial PERC cells positioned according to the thinner being the first to receive the laser beam. The purpose of this architecture is to decrease the load of an individual cell by decreasing the absorption, letting a portion of light get transmitted and increase the overall efficiency by increasing the absorbed efficiency multiple cells. When compared to multi-junction cells, this design can enable greater heat dissipation since the thin cells have a gap between each other where air can circulate. The design was studied with series and parallel connections under varying wavelength and intensity.

In order to study the behavior of different wavelength light near the bandgap energy when high power laser beam is incident to this novel design, a wavelength tunable laser in the range 1030 nm to 1080 nm was built. Since the high-power beam causes a fluctuation in the temperature as well, it is a matter of investigation to determine which wavelength will result in the optimal transmission ratio resulting in a more stable thermal state and thus providing the highest efficiency.

The cells were placed so that the laser beam is incident to the thinnest cell first and then propagates towards the thickest cell placed at the most rear (Figure 4.10 (a,b)). The fabricated cells were named as G5, G4, G3, G2, G1 where "G" stands for "Group". Each group has a specific wafer thickness. G5 is the thinnest (130 µm) and goes thicker towards G1 (which is the thickest cell, 170 µm) by increasing 10 µm in each consequent group (Figure 4.10 (c)).

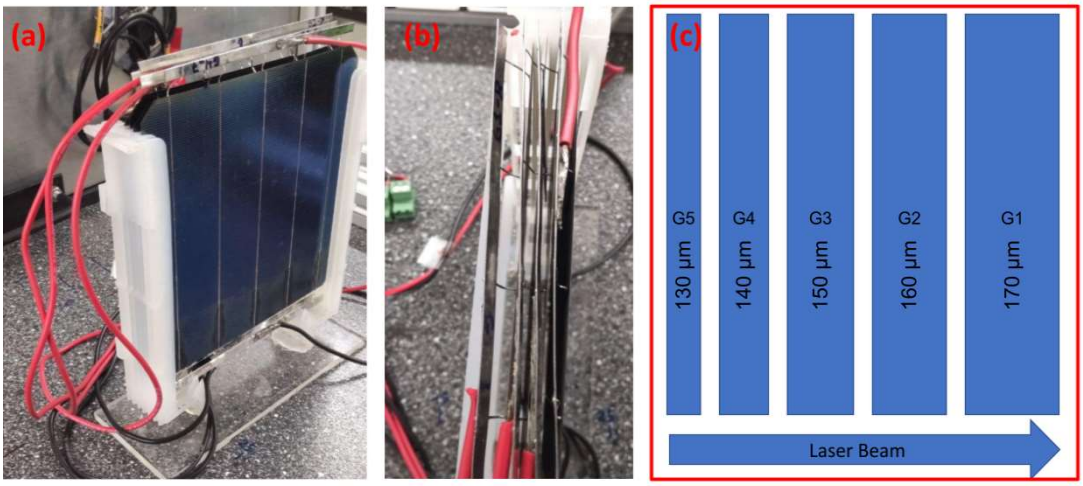

Figure 4.10. (a) Thin PV elements positioned one after the other, (b) A close-up on the thin cells, (c) Illustration of the cells' positions with respect to the beam direction with the cell thickness denoted

In order to evaluate the effectiveness of this design, a new definition of efficiency was made as the "absorbed efficiency". It is basically calculating the efficiency with respect to the absorbed optical power rather than the incident one. An example calculation for the absorbed efficiency is provided in Figure 4.11 for the case when 6 W of 1060 nm laser light is incident. P_{el} is the electrically generated power, P_{in} is the incident power and P_{out} is the transmitted and outgoing power propagating towards the rear cells.

$$Absorbed\ Efficiency\ for\ G4 = \frac{\mathbf{P_{el}}}{\mathbf{P_{in}} - \mathbf{P_{out}}} = \frac{0.17}{3.19 - 1.58} = 10.6\%$$

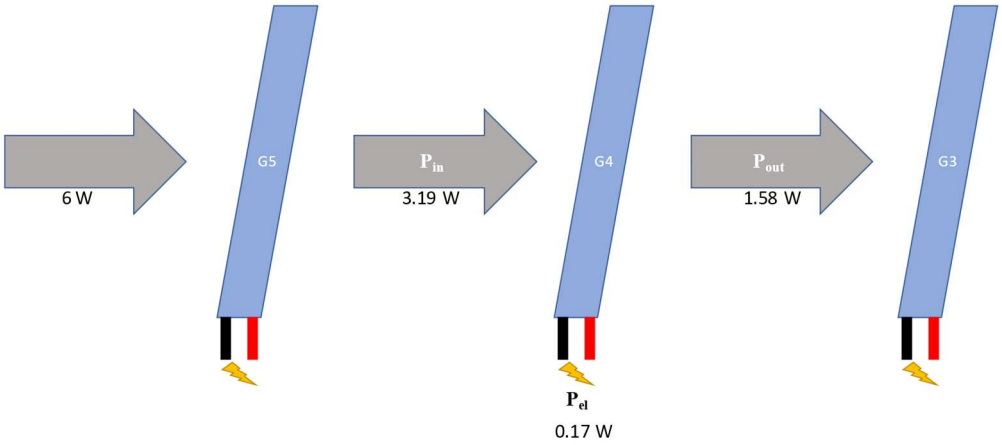

Figure 4.11. An example calculation for the absorbed efficiency presented with incident power 6 W. 53.1% of incident light is transmitted from G5 to G4 which is equal to 3.19 W, this optical power incident on G4 is defined as P_{in} when calculating absorbed efficiency for G4. 49.4% of P_{in} is equal to 1.58 W and transmitted to G3, this transmitted part is defined to be P_{out}. While the cell G4 was generating 0.17 W of electrical power and defined to be P_{el} absorbed efficiency is equal to 10.6%

Prior to the absorbed efficiency calculations, each cell of different thickness had their transmission measured under 4 W of 1060 nm light. This was done by measuring the laser beam intially with a powermeter and then placing the desired cell in front of the powermeter and measuring the power transmitted after the cell. However, an important detail to be noted, it was observed that as the incident power increases, the cell was heating up and its transmission was decreasing, resulting in greater absorption. As the power increases, the transmission is dropping much faster in a few seconds after placing the cell. For example, the frontest cell, G5, (Figure 4.18) transmitted 2.30 W of the 4.05 W of incident power at the first instant it is placed in front of the laser beam. In less than a second it dropped to 2.15 W and kept having a very slow transmission decrease afterwards that is slow enough to be considered stable. The rest of the cells were also showing this behavior and 4 W is providing an intermediate value for the powers from 2 W to 8 W. After 4 W it was not possible to

find a stable transmission, due to high temperature rise on the cell and rapid fluctuating heat transfer, the transmission was showing very fast changes.

For the absorbed efficiency calculations, the same transmission has been assumed for the different powers. Under these conditions, the transmission of the first cell (G5) was 53.1%, gradually decreasing with each cell until 39.5% transmission at the last cell (G1) placed at the most rear.

While calculating the absorbed efficiency using the transmission values, the power transmitted from the cell was calculated which the laser light first passes through. This light that has passed through the first cell becomes the incoming power for the second cell. When calculating the efficiency of the second cell, the light that is transmitted through the second cell is subtracted from the light that was incident on it, and the electrically generated power by that cell is divided to this absorbed power.

It was not possible to measure the reflection of the cells due to the light getting scattered too much after incident to the cell surface. The present powermeter had its opening for entering light much smaller than the reflected light area. So, if it was possible to measure the reflected light, it would be possible to calculate the absorbed power more accurately and thus obtain greater absorbed efficiency values. However, under these conditions, it was neglected in the calculations, if it was known, it was going to be subtracted from the incident power term just like the transmitted power term, giving us the true absorbed power.

By absorbed efficiency calculation it is possible to have a measure of how effective an individual cell is and comment on the overall properties of the novel thin multi cell design. The total sum of each of the cell's individual absorbed efficiency also provides information about the overall performance even though it does not provide information about any physical variable.

CHAPTER 5

RESULTS AND DISCUSSION

The structures introduced in Chapter 4 were experimented with and the results are presented in this chapter. Initially the simulation aided monofacial PERC cell results are presented. Then, the thin multi-cell design established with the bifacial PERC cells are presented and a second PV cell structure is introduced, interdigitated back contact (IBC). This structure is also studied in multiple aspects including illuminating with double beam and the effects of shadowing. Later, a panel is fabricated with IBC cells and experimented with. Comments regarding the factors affecting the efficiency results and how they can be improved in future work are also included as a discussion. Finally, the field experiment is presented with future goals.

5.1 Wire-grid Optimized Monofacial Cells

The highest efficiency cell design obtained according to the simulation was fabricated and resulted in 28.12% efficiency under 1060 nm light incident with 2.801 kW/m^2 intensity. It was converting 880 mW optical power to 247.5 mW of electrical power. One of the key factors causing an efficiency lower than the simulation results was the metal contacts made between the measurement system and the cell. It was not possible to produce metal contacts for this cell at the GUNAM facilities and custom ways of establishing contacts were tried. The best method possible was drilling an aluminum plate and fixating the cell to the plate by plastic screws (Figure 5.1). Still, it was not behaving ideal due to the resistance and was causing ohmic behavior on the IV curve at higher currents. The IV curves and characterization of the cells were done with a custom built IV measurement system. Its working mechanism is explained in Appendix A.

Just like the quality of contacts made between the PV cell and the measurement system, Griddler was not capable of calculating many additional parameters' effect. The unaccounted parameters include the temperature rise on the cell under high intensity light or the resistance between the cell and electronic measurement system resistances in addition to the quality of contacts. Thus, the obstacles for reaching the simulated efficiency needs further improvements on the system and the simulation needs to account for more parameters.

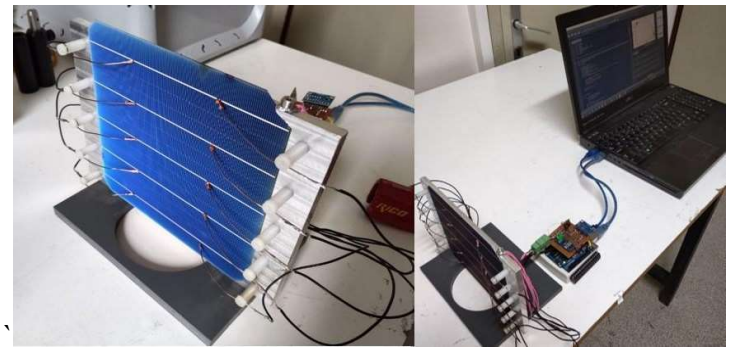

Figure 5.1. Images of the custom-built photovoltaic cell holder (close-up on the left) and the IV characterization setup (on the right) including the cell, its holder, electronic measurement system and the PC used for running the python code

With this technique, the cells with a novel design were characterized when laser light of 1060 nm is incident as simulated in Griddler. The cell was incident at varying powers and beam diameters. The 1060 nm light was obtained from the tunable laser fabricated. It was tuned to 1060 nm and the monofacial PERC cell fabricated at ODTÜ-GÜNAM was used. With the holder made, the cells were studied under 1 cm and 2 cm beam diameters with power varying from 0.73 W to 1.36 W (corresponding to intensity range 2.64-3.50 kW/m^2) where a peak in the efficiency could be observed providing the highest value and gradually decreasing after the peak. The highest efficiency was measured as 28.1% under 2.801 kW/m^2 intensity with a 2 cm beam diameter. The efficiency vs. intensity graph can be seen in Figure 5.2. The process of obtaining beam diameters is done via digitizing the IR image of a beam and obtaining its Gaussian profile. This process is explained in more detail within Appendix B.

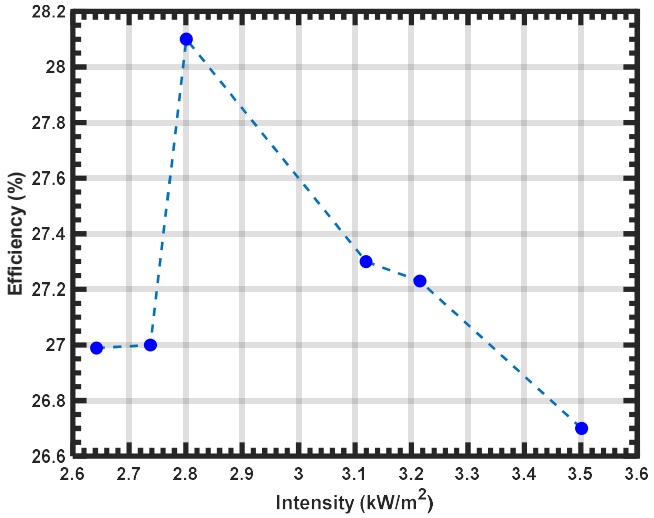

Figure 5.2. Efficiency vs. Intensity of monofacial PERC cell under laser beam of 1060 nm

5.2 Thin Multi-Cell Structure

The cells were initially studied at low power (until 1.6 W) and then with higher power (greater than 1.6 W). Data for 1.6 W can be observed in Table 5.1 for parallel, series and individual measurements and high-power measurements data is presented in Figure 5.3 for parallel and series connections. The lower powers until 1.6 W is also included in Figure 5.3. Parallel connections were showing the same trend with individual measurements of each cell under the change of wavelength; higher efficiency was obtained as the wavelength gets shorter. The measurement system was able to measure parallel connections precisely, however, this was not possible for the current provided by the series connection of the cells. They provided currents at the order of measurement system's error (±100 mA) and even lower. Thus, great noise was being present, it was not possible to obtain precise results.

Table 5.1 Efficiency of each cell measured individually, in parallel and series connections under varying wavelengths of 1.6 W light from 1030 nm to 1080 nm with beam diameter 2.5 cm

Wavelength	*Parallel*	*Series*	*G5*	*G4*	*G3*	*G2*	*G1*
1080 nm	5.0%	3.4%	1.3%	2.2%	1.4%	1.1%	1%
1070 nm	6.3%	4.8%	2.4%	2.3%	1.2%	0.6%	0.7%
1060 nm	7.9%	5.7%	2.4%	2.8%	1.1%	0.7%	0.7%
1050 nm	8.3%	4.3%	2.8%	3.2%	0.9%	0.4%	0.3%
1040 nm	8.9%	5.7%	3.6%	3.3%	0.9%	0.6%	0.6%
1030 nm	9.3%	0.6%					

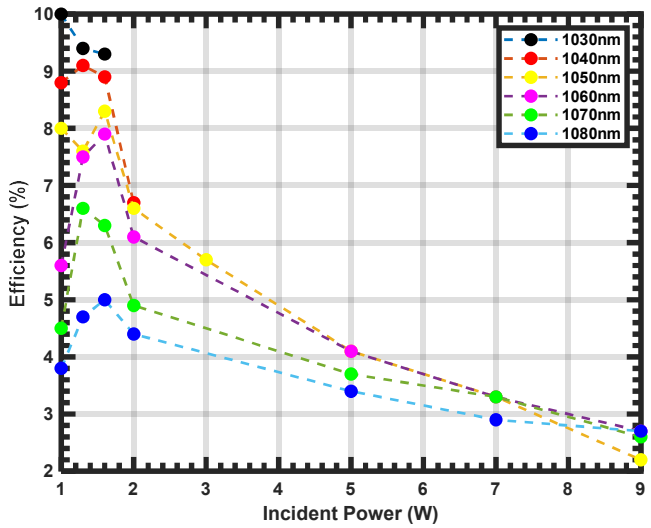

Figure 5.3. Efficiency vs Incident Power for Thin Multi-Cell stack with higher power, connected in parallel, having 2.5 cm beam diameter

Nevertheless, it can be concluded from the parallel connection results that the maximum efficiency is observed at smaller wavelengths, 1030 nm in the experiments. The laser beam was set to 2.5 cm beam diameter and 1.6 W of optical power, corresponding to 3259.5 W/m^2 intensity. The calculated absorbed efficiencies are provided in Table 5.2 for various beam diameters.

At 5.61 W and 2.3 cm beam diameter, even though the power is higher and the beam diameter is smaller compared to 1.6 W and 2.5 cm beam diameter (which implies greater intensity and more heat buildup causing less transmission) the overall absorbed efficiency has the greatest value. This can be caused by the smaller beam incident on the first cell being subject to less scattering and providing more light to the cells behind.

Table 5.2 Calculated absorbed efficiency of each cell by making individual measurements, under varying beam diameter and beam power

Beam Diameter	*Power*	*Total*	*G5*	*G4*	*G3*	*G2*	*G1*
2.5 cm	1.6 W	46.30%	5.10%	10.40%	6.94%	5.80%	18.10%
1.3 cm	1.98 W	48.55%	5.49%	11.66%	8.99%	10.24%	12.17%
2.3 cm	3.76 W	55.32%	6.12%	12.67%	12.42%	11.20%	12.89%
2.3 cm	5.61 W	55.84%	5.72%	11.40%	12.31%	17.65%	8.74%
2.3 cm	7.48 W	49.12%	4.12%	9.27%	11.73%	13.42%	10.56%

Throughout these measurements, the light was scattering too much while getting transmitted through the cells when inspected with an IR camera. This does not enable preserving a constant beam diameter. Thus, a means of minimizing the scattering needs to be developed for improved light transmission and efficiency. A new design of cell holder that will keep the cells as a stack but with less spacing in between cells can be studied in future work. This new design can also employ a means of temperature regulation via integrating a cooling fan for keeping the transmission more stable as well. This way, both regulating the temperature and minimizing the scattering would be accomplished and much higher efficiencies can be obtained.

5.3 IBC Cell Structure

In addition to the thin multi-cell design, additional experiments were done by studying a PV cell with interdigitated back contact (IBC) structure. To the best of

our knowledge, the IBC structure was not studied for power beaming purposes before except for this study. In the latter of this section, the IBC cell is investigated and the findings about it will be presented, then some additional techniques related to the laser beam such as multi-beam and shadowing of the outer part of the beam area will be explained with the experimental findings, and finally its field experiment results will be presented.

It was seen in the experiments that an IBC structure can provide higher efficiencies with a single cell with respect to PERC structure. In order to study its behavior under various configurations for power beaming, it was studied with varying wavelength, beam area and beam power. It must be noted here that varying the beam area and power does not result in the same physical change by varying the intensity. This finding will be explained in the following pages.

The efficiencies when illuminated with beam diameter of 2 cm and varying power until 10 W can be seen in Figure 5.4. IBC structure also follows the general trend, the efficiency is higher as the wavelength gets shorter. The small deviations from the general trend that are observed at higher powers can be caused by the thermal effects on the cell. As the beam is incident, the cell temperature starts rising. At that state, even the rate of air circulation inside the laboratory environment can slightly affect the heat transfer and the measurements. In order to eliminate this, a temperature stabilization system is planned to be implemented. The fluctuations observed until 1.6 W are related to the current provided by the cell being close to the measurement system’s current error.

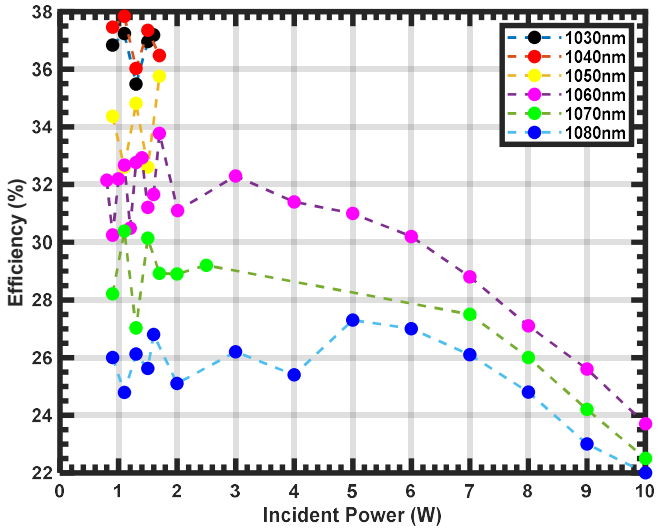

Figure 5.4. Efficiency vs Incident Power for IBC cells under 2 cm beam diameter of various wavelengths

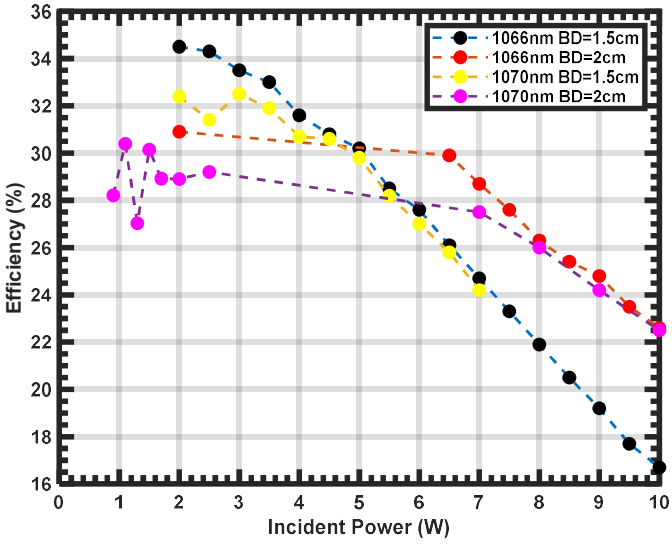

Figure 5.5. Efficiency versus Incident power for 1066 nm and 1070 nm of 1.5 and 2 cm beam diameters (BD: Beam Diameter)

The varying beam area in Figure 5.5 shows that there is a specific beam power at which two different beam diameters provide the same efficiency. However, if the beam area is increased while also increasing the beam power and reaching the same intensity, the same efficiency cannot be obtained. So, the efficiency does not depend on intensity solely. This is the same case for every wavelength experimented with.

Hence, the cell design must be done by taking into account the total power it is intended to generate and the intended area of the beam rather than only considering beam intensity.

Another experiment involving the beam area and power together being doubled to show this effect was conducted. First the power and beam area were doubled, then both of them were made four times the initial power and initial area. In all of them the intensity was approximately kept the same.

2 W of 1050 nm light was incident on an area of 0.000252 m^2, having 7936 W/m^2 intensity, resulting in 26.3% efficiency. Then the power was raised to 4 W and area to 0.000526 m^2, intensity being 7598 W/m^2, it provided 28.3% efficiency. Then raised the power to 8 W and area to 0.000989 m^2, intensity being 8090 W/m^2, it provided 24.6% efficiency. So, it can be concluded that the same intensity does not provide the same efficiency and the total power incident must also be taken into account.

Another experiment's results involving the comparison of the efficiencies between 1050 nm and 1060 nm light, both with 4 W of power can be seen on Figure 5.6. It was plotted with respect to the beam area. The intensity is shown on the right y-axis with red color data and efficiency values are on the left y-axis with blue and black colored data points. The area denoted in the x-axis was the beam area obtained when the cell is positioned at 20 cm distance from the laser system, going until 130 cm distance under that lens alignment. The area on the Figure 5.6 marked on the x-axis and the distance on the Figure 5.7 marked on the x-axis coincide with each other, corresponding to the same configuration of the cell distance and beam area.

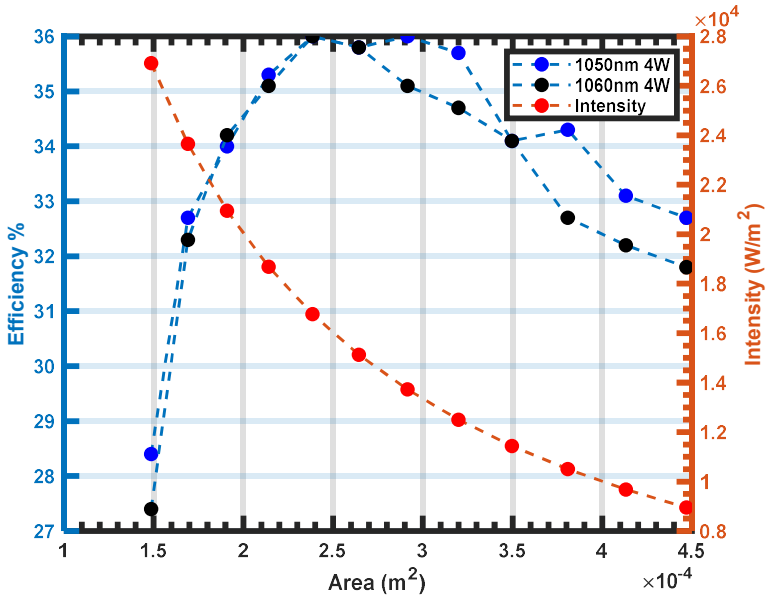

Figure 5.6. Efficiency versus Beam Area with 4 W laser illumination of 1050 nm and 1060 nm (red data representing intensity via right y-axis)

The trend seen on Figure 5.6 is, as the beam area is increased under constant power, the efficiency starts from a relatively low value, then increases until a peak point, then decreases gradually. From left of the graph to the right, the intensity is gradually decreasing while the beam area is gradually increasing with beam power being constant. The efficiency of 1050 nm is slightly higher overall, following the trend observed on Figure 5.4.

When the results obtained with 4 W are compared with the 2 W of light of the same wavelengths presented in Figure 5.7, it can be concluded that the cells are providing better efficiency at lower powers in addition to shorter wavelengths.

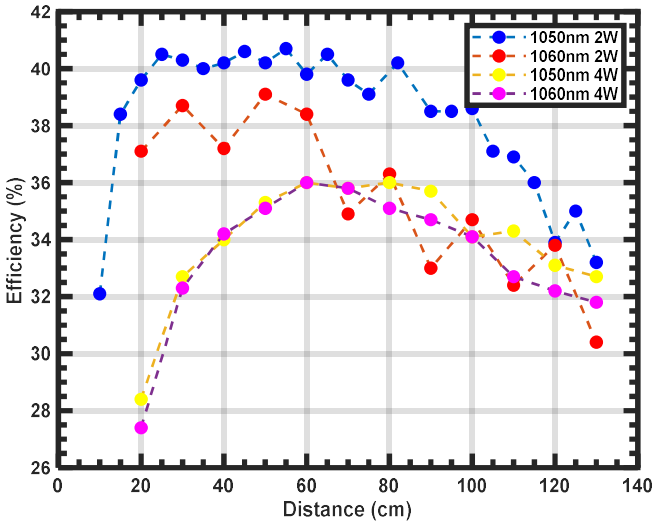

Figure 5.7. Efficiency versus distance with 2 W and 4 W light for different wavelengths (the distance values coinciding with the area values of Figure 5.6)

An observation at higher powers was the immense heat produced at the cell where the beam is incident on. At the power levels where power is coming closer to 4 W, the rising temperature of the cell can be felt by hand when touching the cell from behind. Near 8 W it feels really hot by hand. The rising temperature implies more recombination and less efficiency, causing a need to dissipate the heat. After this observation, the IBC cell was glued to an aluminum plate with thickness of 1cm for increasing the heat dissipation and the efficiency. The glue used was a special polymer that was manufactured with high thermal conductivity for the specific purpose of better heat dissipation. It was observed that at lower powers, the aluminum plate does not affect the efficiency considerably. However, as the incident power is increased, the aluminum plate and high thermal conductivity glue increases the heat dissipation and keeps the efficiency higher with respect to non-aluminum plated IBC cell. There was an approximately 2% increase of efficiency at 8 W when the aluminum plate was present (Figure 5.8). The beam had a FWHM 2.08 cm beam diameter kept constant, and its intensity varied from 2934 W/m^2 (at 1 W) to 23468 W/m^2 (at 8 W). This experiment has also provided evidence that heat buildup on the cell is causing more recombination and thus decreasing the efficiency. In future

work, holes can be drilled to the aluminum plate and water can be cycled through the holes for improved cooling.

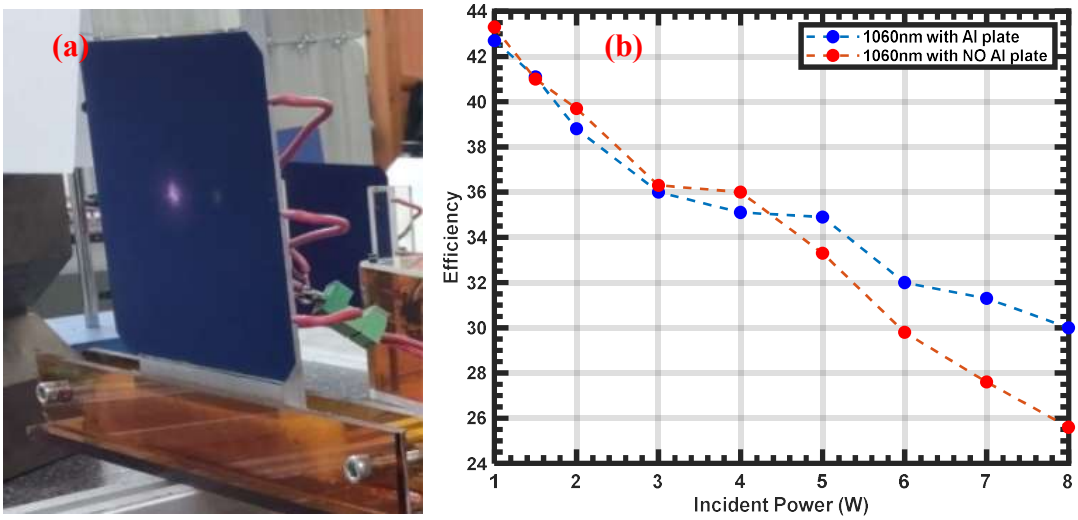

Figure 5.8. (a) Image of an IBC cell glued with high thermal conductivity glue to an aluminum plate, (b) Efficiency vs Power graph with and without the aluminum plate glued to the IBC cell under laser beam with 2.08 cm FWHM beam diameter and 1060 nm wavelength

Another observation was the effect of wavelength diminishing at higher powers. This was observed with 1050 and 1060 nm of light, under fixed beam diameter (corresponding to 2.25 cm FWHM beam diameter). The graph is presented in Figure 5.9. It was observed that, as the incident power increases and the efficiency drop becomes considerable, the difference between both of the wavelengths becomes negligible. This may indicate that the cell is reaching the limit of its design's electrical properties and electrical properties become dominant. In that case, the efficiency difference caused by the optical properties becomes negligible.

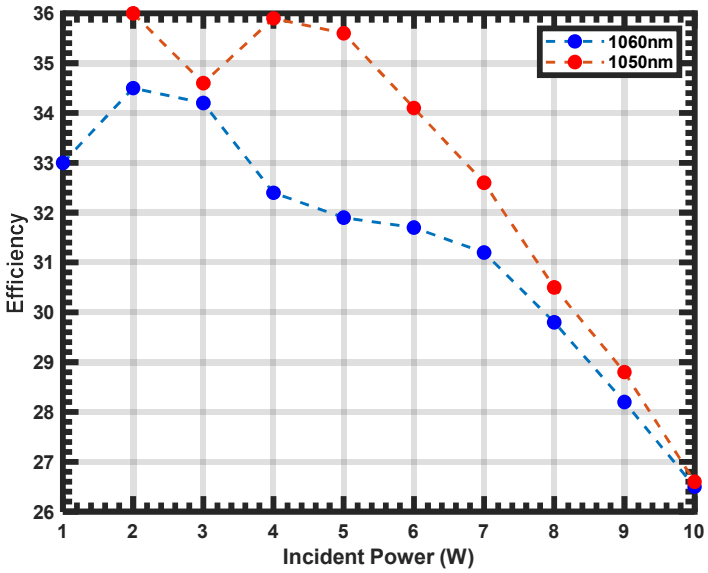

Figure 5.9. Efficiency versus Power with 2.25 cm FWHM beam diameter for 1050 nm and 1060 nm

Using this observation, a comment can be made on mentioned effect of different beam area and power having the same intensity not resulting in the same efficiency. It can be caused by two aspects; the total beam power is coming closer to the electrical limit of the cell and electrical properties becoming dominant, or, different regions of the photovoltaic cell lacking impedance matching. A PV cell has its resistance changed dependent on illumination parameters. The cell can be modelled as resistances connected in parallel and these resistances may cause a loss in efficiency because of lacking impedance matching. It is a common technique in power electronics to match the impedance of resistances and an energy source connected in parallel for maximizing their load carrying efficiency. In the case of a PV cell, different beam areas would be activating different amounts of the cell area, resulting in a different impedance with respect to the inactivated area. The highest efficiency found can be corresponding to the impedance value that is matching the rest of the cell's impedance which does not have light incident on. If it is tried to illuminate all of the cell area with greater power for obtaining the intensity, then the non-matched impedance can be the cause of not being able to get the same efficiency

under the same intensity. This hypothesis can be supported by the results of the next section “Effects of Shadowing”.

5.4 Effects of Shadowing

Effects of illuminating different cell regions was investigated by shadowing the cell area surrounding the laser beam. This way, a specific area is activated by very low-power laser light, hypothesized to be changing that local region’s resistance. This is done without changing the main beam intensity which carries 99% of the power.

By the aid of an IR camera, it is possible to increase the exposure time to see the very low intensity laser light incident on the cell. This level of very low power light cannot be seen with an IR detector card or a smartphone camera. It was only possible when the scientific IR camera’s exposure time is increased considerably. It is very low power but can activate the local area it is incident on, changing its resistance and the rate of impedance matching with the other local areas of the cell. Figure 5.10(b) shows the image taken with the IR camera when its exposure time is set to maximum, while Figure 5.10(a) shows the calibrated power level image which the beam diameters are obtained from. The colored image on Figure 5.10(c,d,e) shows the beam images taken by a smartphone/tablet camera. The laser beam is still visible but looks much dimmer compared to the IR camera.

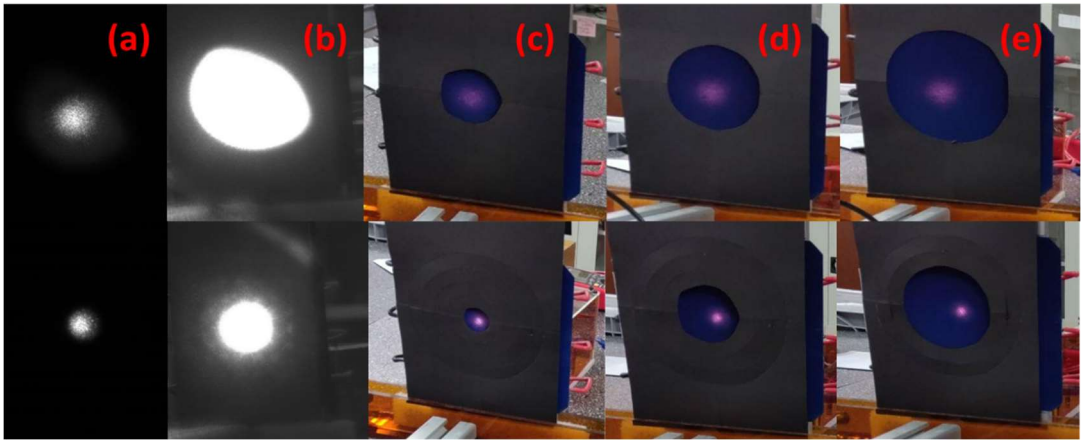

Figure 5.10. (a) The power calibrated IR image of the 2 cm diameter beam at top and 1 cm beam at the bottom, (b) the same beams with the same scale but with maximum exposure time, 2 cm diameter beam at the top and 1 cm one at the bottom, (c) smartphone camera image of the same beams sent through 4 cm of opening (top) and 2 cm opening (bottom), (d) 6 cm opening on top and 4 cm opening on the bottom (e) 8 cm opening on top and 6 cm opening on the bottom

The experiment was done by providing shadowed region around the area covering the beam so that the small intensity light does not reach the cell surrounding the beam. A black paper was used to provide shadow. The circle cut from the black paper provided an opening for the main power carrying beam to reach the cell while the low intensity lights surrounding it were blocked.

Firstly, a beam of 1050 nm and 2 W power with 2 cm beam diameter is sent through a 4 cm diameter opening of a black paper. The efficiency is measured at that configuration and without changing any of the parameters, only the opening of the black paper was increased to 6 cm diameter, then to 8 cm, then to 10 cm. The same procedure was applied to a beam of 1 cm diameter as well, starting with an opening of 2 cm diameter on the black paper going until 10 cm. Results are shown in Table 5.3.

It can be seen from the table that, as the low-intensity light around the beam is increased by cutting more area on the black paper, the optical to electrical conversion efficiency was also increased. The increase in efficiency continues until the paper

opening area reaches the low-intensity light area that is seen in Figure 5.10(b). After that point, increasing the black paper opening area does not have any effect on the efficiency while the low intensity light area is completely inside the black paper opening and constant.

Table 5.3 The efficiency obtained in the shadow experiment for two beam diameters and varying black paper opening diameters

Beam Diameter (below)	*Opening Diameter (right)* →	*2 cm*	*4 cm*	*6 cm*	*8 cm*	*10 cm*
2 cm	Efficiency (right) →	-	34.0%	37.9%	39.8%	39.1%
1 cm	Efficiency (right) →	25.4%	25.8%	26.2%	26.0%	26.2%

In addition to this varying black paper opening area experiment, another observation was made while working with an additional lens placed in front of the beam. The lens was causing a ring of shadow around the main beam carrying 99% power. An observation was made when the lens shadow ring is present and when it is not while the beam diameters are adjusted to have the same value in both cases. The lens was initially positioned outside the laser system for the purpose of changing beam area much more easily in small distances within the laboratory.

Similar to the shadow experiment, an increase in the efficiency was observed when the area around the beam is illuminated with low power light and shadow is not present. The efficiency increase was calculated to be more than the power that the low intensity light was carrying. The setup is illustrated in Figure 5.11.

The observation was made with 2 W of 1060 nm light incident on the cell when there is a focusing lens in front of it and when there is not. The lens distance is adjusted so that the beam diameter is the same in both of the measurements (FWHM is equal to

1.46 cm when there is no lens, and 1.41 cm when there is lens, they were adjusted to the same value as much as possible).

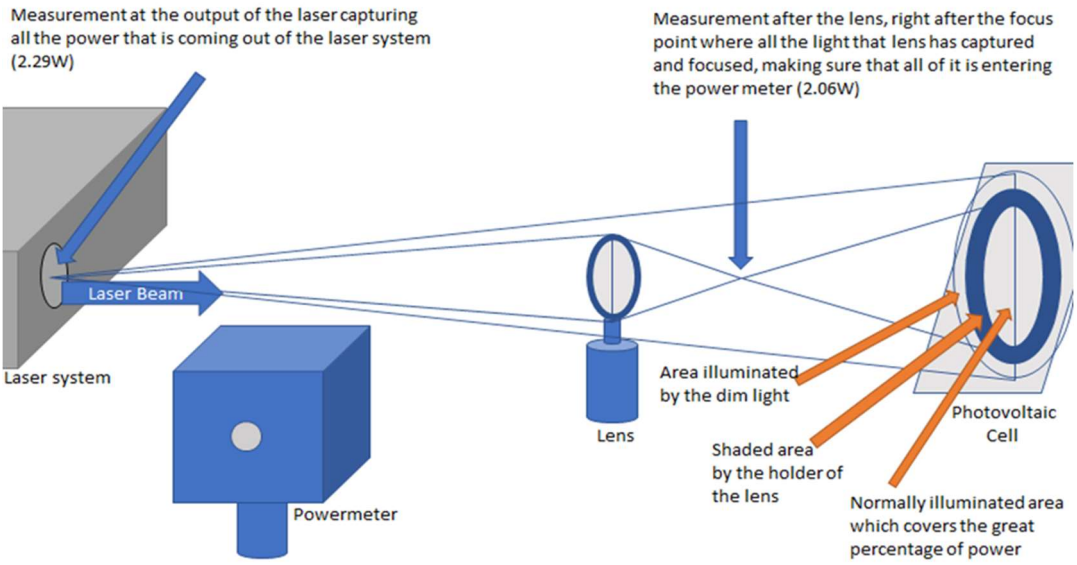

Figure 5.11. Setup illustration for the shadow experiment with explanations

In the case where there is no lens, the power is measured from the output of the laser system, which was 2.03 W and an efficiency of 33.3% was measured. In the case where the lens is present, the power is first measured from the laser output and then after the lens. All of the power coming from the core of the laser's final amplifier fiber was entering the lens with a very small diameter compared to the cladding light. Some of the cladding light was getting scattered and forming a large and low-intensity illumination circle around the core light at the center with a smaller diameter which can be observed in Figure 5.12. The two images in the middle of the figure is showing the main beam with 99% power. No scattered low-intensity light can be observed at these images where the camera is calibrated for obtaining the calibrated Gaussian beam profile implying the power contained by the low-intensity light is zero with respect to calibrated configuration. It can be showed by calculating the main beam power from equation 5.1 that 99% of the power of a gaussian profile is contained within the 1.52xw= 1.52x(FWHM/ (sqrt(2xln2))), where w is the 1/e2 beam radius and FWHM is the full-width half-max radius of the beam. The 99%

power containing diameter is calculated to be 2.61 cm (in terms of 1/e2) for the beam used in this experiment having FWHM=1.46 cm (1.72 cm in terms of 1/e2 beam diameter).

$$P(r,z) = P_0\,[1 - e^{-2\,r^2/\,w^2(z)}] \tag{5.1}$$

where r is the radius of interest, P_0 is the total power of the beam and w(z) is the beam radius defined by 1/e2 of the beam.

The illuminated area by the light passing through the lens can be observed as the bright circle located at the center on Figure 5.12(a). It is much greater than 2.61 cm (greater than 5 cm). The beam without a lens can be seen in Figure 5.12(b). With these considerations, the power measured right after the laser output was 2.29 W. After the lens, near the focus point, making sure that all the light that lens is capturing enters the power meter, it was 2.06 W and the efficiency was measured to be 24.2% at the cell. So, the total optical power of bright light at the center is 2.06 W and by inspection of the IR image, a great portion of the power difference (2.29-2.06=0.23W) was propagating outside the cell and not being incident at all.

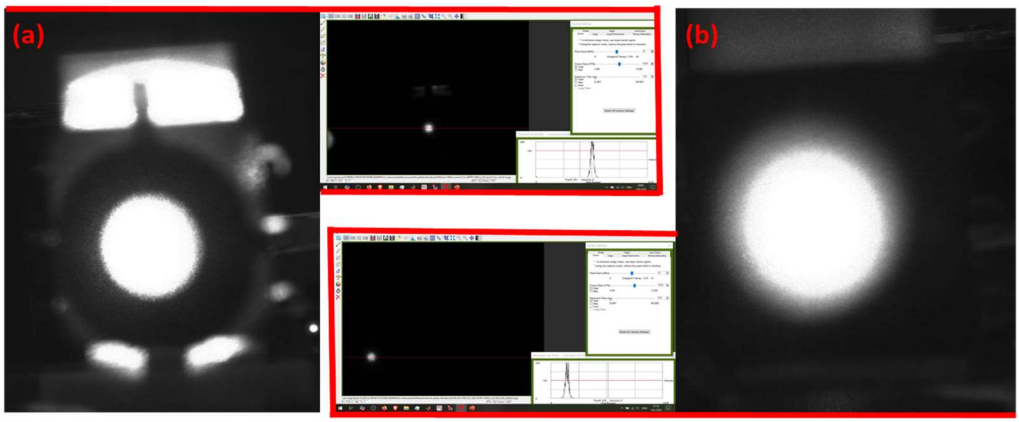

Figure 5.12. (a) The shaded configuration on left with maximum exposure time enabling low-intensity light to be visible and its power calibrated image on its right (top middle column), outlined with red (b) The non-shaded configuration on right and its power calibrated image on its left (bottom middle column), outlined with red

In both cases, the power that reaches the cell surface is approximately 2 W but, in the no-lens case, the diffused light was not blocked by the lens. For the case where lens is present, the power measured at the output of the laser beam had 0.23 W of extra power which can be hypothesized to be partially reaching the cell from the outer area around the lens shadow, but even if all of that light were to reach the cell, it would cause 0.23 W x 0.333=0.0759 W (without the lens it was 33.3% efficiency so assuming the same efficiency) to be generated. 0.0759 W/2.06 W=0.0368% (3.68%), which is (33.3-24.2=9.1%, 9.1-3.68=5.4%) 5.4% less than the measured increase.

So, since the optical power that is not collected and not focused by the lens does not have enough power for generating that increase in efficiency, it is indicating that there is an effect after the absorption of light on the cell. This property can be investigated using the Standard one-diode-model widely used for solar cells as shown in Figure 5.13. In future work, an experiment regarding whether the data from simulating impedance matching through this model is in accord with the measured values or not can be conducted. The simulation data can be compared with a dataset including greater variety of parameters. This includes, varying the power of the dim light activating the area around the beam center, trying different shapes of shadows and using the simulation results of impedance matching for finding a method of calculating the optimal shadow of a cell design. The double beam concept presented in the next section can be used for varying the power of main beam and the low-intensity light.

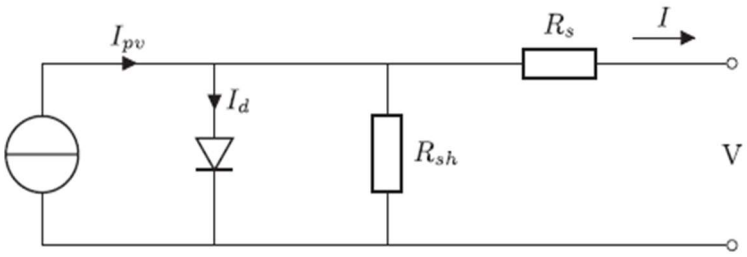

Figure 5.13 An illustration of the Standard one-diode-model widely used in Solar research [60]

5.5 Effects of Double Beam

Another method that was experimented with is, increasing the number of beams incident on the cell. This was done by placing a beam splitter and a mirror in front of the laser beam. The setup can be seen in Figure 5.14.

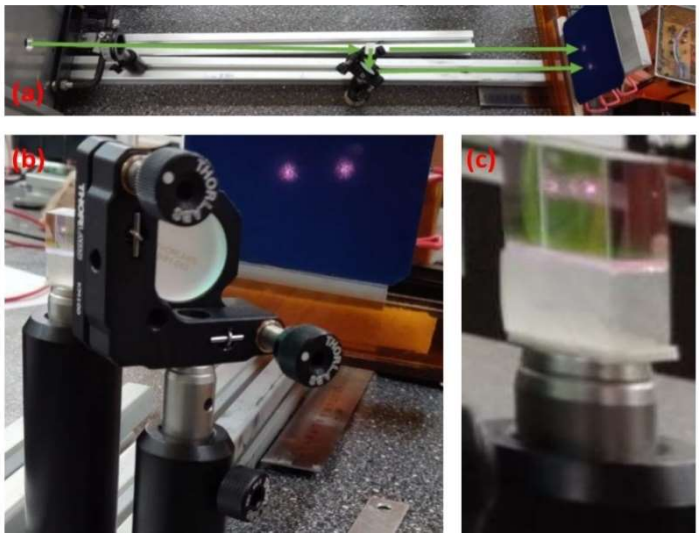

Figure 5.14. (a) The setup for splitting the beam and obtaining a double beam. (b) Close-up on the beam splitter and adjustable mirror. (c) Zoomed-in Beam Splitter

The incident single beam was at 1060 nm with a 1.24 cm FWHM beam diameter. For the double beam, it is the total power of the beams which the efficiency is calculated with respect to. When the left beam only (having 1.65 W of optical power) was incident 31.0% efficiency was measured (Figure 5.15(a)). This beam is the stationary beam positioned at the center. When the right beam only (having 1.72 W of optical power) was incident 19.6% efficiency was measured (Figure 5.15(c)). This beam is the directable beam whose position can be adjusted. And the double beam carrying, 3.47 W, has provided 22.8% efficiency (Figure 5.15(b)).

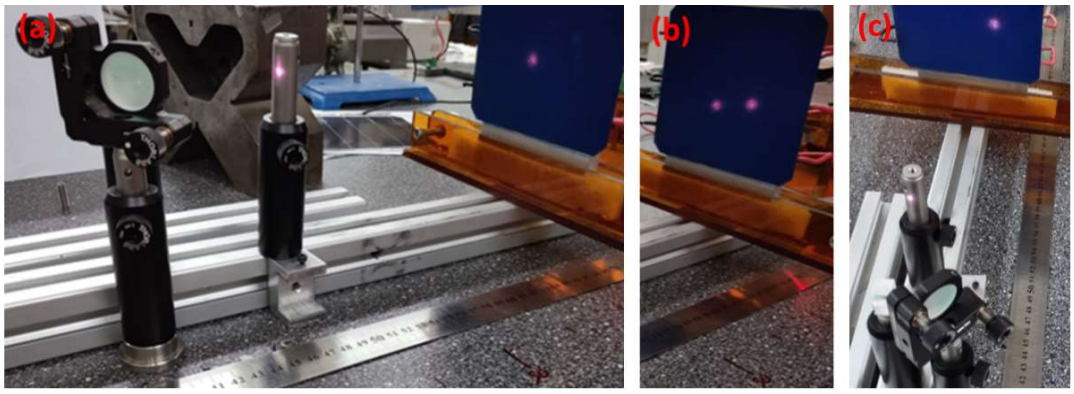

Figure 5.15. (a) Only the left and fixed beam incident with 1.65 W (b) Both of the beams are incident with 3.47 W total (c) Only the right and moving beam incident with 1.72 W

The experiment was also conducted for 5.6 W of power divided into two beams. In this case, the fixed beam was positioned ~3 cm above the center (providing 2.79 W) resulting in 28.9% efficiency and the moving beam alone was positioned at the center (with 2.82 W) resulting in 31.2% efficiency. When both of the beams were incident at their same location (a total of 5.61 W) the efficiency was 25.2%.

So, taking Figure 5.4 as reference as well, dividing a beam of 5.6 W or a beam of 3.5 W into two beams did not increase the efficiency either. Both of the powers as a single beam provided ~32% efficiency in Figure 5.4 but when they are divided into two beams, 5.6 W resulted in 25.3% and 3.5 W resulted in 22.8%.

Thus, dividing the beam into two did not increase the efficiency, however it can be a method for increasing the efficiency of a panel made of many cells. As it will be explained in the next section, a panel fabricated with IBC cells under a gaussian beam results in the efficiency that is much lower compared to the individual cell measurements with a smaller beam and greater intensity with the same optical power incident. So, a multi-beam approach can be investigated for such an application. At the same time, this provides supporting evidence to the earlier conclusion, total power a cell will be receiving needs to be considered when designing a power beaming receiver rather than only considering the light intensity.

5.6 IBC Panel

A panel was built with IBC cells with twenty five IBC cells fixed to an aluminum plate of thickness 8 mm by using the high thermal conductivity glue mentioned earlier. The panel can be seen in Figure 5.16(a,b). The cells were studied under varying beam power, beam diameter and measurements were completed under different connections (parallel, series, individual).

Beam diameters were measured as explained in Appendix B; the IR image obtained by the scientific camera is digitized and a colormap of the image is obtained in addition to the FWHM calculation. This is beneficial for visually inspecting the beam distribution more effectively. An example can be seen in Figure 5.16(c,d) . When there are too many speckles due to scattered light, a Gaussian fit is applied. Then the FWHM is obtained from the Gaussian fit.

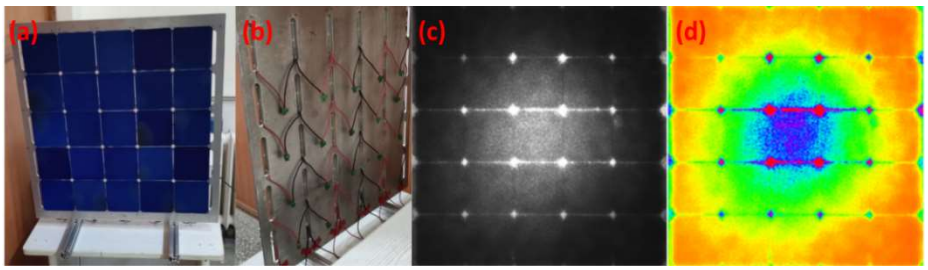

Figure 5.16. (a) IBC Panel (all cells covering 62.5 cm x 62.5 cm area) shown from front and (b) shown from the backside (c) IR image of laser beam incident on the panel and (d) its colormap image

Initially the panel was experimented with 4,7 and 10 W of optical power at 1060 nm. Each column of the cells was connected in parallel and then measured as individual column connections. The efficiency with respect to the total optical power sent is illustrated below each column on Figure 5.17. Then, these columns were connected in parallel and series and the measured efficiencies are presented next to the colormap of the cell on Figure 5.17. The beam had 33 cm FWHM diameter.

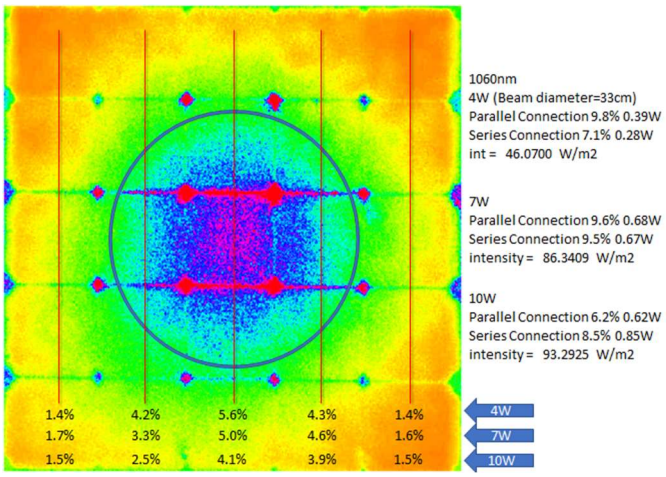

Figure 5.17. Efficiency of each column of cells (cells in the column connected in parallel), and columns connected in parallel and series with each other noted on the right of the colormap

Although the beam intensity is much less with respect to the single cell measurements presented in Figure 5.4, the individual efficiencies of IBC panel columns were relatively lower than single cell measurements. Each of the columns had their peak efficiency in different beam powers so they cannot be directly connected in parallel or series, there needs to be a power optimization circuit designed. The middle column had its greatest efficiency with 4 W beam while the other columns had their peak efficiency under 7 W beam. While the parallel connection of the columns with each other is approximately the same for 4 and 7 W beam (~9.7%) but shows a great drop under 10 W to 6.2%. The series connection of the columns on the other hand shows a peak at 7 W resulting in 9.5% efficiency and decreasing for both lower and greater power beams.

In order to check whether individual cells were functioning properly, they were desoldered from the panel and their efficiencies were measured with a much smaller beam diameter laser beam directed on a single cell (Figure 5.18(a)). This way it can be studied whether the reason is light intensity and connection of the cells, or the cells have a manufacturing fault. 1050 nm light of 2 W power was sent with 1.66 cm FWHM beam diameter to individual cells of the middle column one by one and

measured individually. This beam power and diameter was providing very high efficiencies in earlier experiments with single cell (greater than 35%), the image of the earlier experiment laser beam is visible on Figure 5.18(b). As it can be seen from the Figure 5.4, their individual efficiencies were much greater under laser beam of smaller area with higher intensity when compared to their performance on the panel.

As shown on Figure 5.18(d) the individual cells have shown much greater efficiency (near 30%) when compared to their parallel or series connection efficiencies on the panel (values between 6.2% to 9.8% seen on Figure 5.17). As a reference, a single IBC cell glued to an aluminum plate with the same high thermal conductivity glue was also experimented with in front of the big panel with the same beam incident (Figure 5.18(c)). It had approximately the same beam area due to being in front of the panel and provided 36.8% efficiency under 2 W of power. The small difference can be caused by the imperfections of each cell's manufacturing processes. A visual observation on Figure 5.16(a) also provides evidence to that by the colors of the cells with some of them having a lighter color and some having a darker color caused by their manufacturing non-homogeneity.

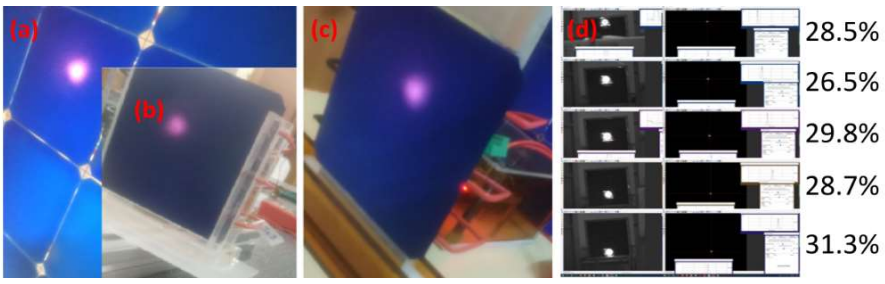

Figure 5.18. (a) Image of the beam when directed to the individual cells (b) The image of configuration when the ~40% efficiency was obtained by single cell measurement. (c) The image of an aluminum plated cell experimented with in front of the panel. (d) 5 images on the left are the beam images with highest exposure time and on the right are power calibrated images, efficiencies are denoted on the most-right of the image

Thus, it can be concluded that the cells do not have a dominant faulty behavior and are able to provide near 30% efficiency with a smaller beam providing higher

intensity. Then, the efficiency drop seen on the panel measurements is related to the optical power distribution and each cell obtaining a different maximum-power-point (MPP) voltage. This is limiting each other in series and parallel connections, causing the potentially generated power to be dissipated before getting harvested. After this finding, raising the power to a greater intensity on the panel and also measuring each cell without being connecting with any other cell (individual cell) were tried. The results of varying beam diameter, power and connection type can be viewed on Table 5.4. These were all completed with 1060 nm wavelength.

Table 5.4 Efficiency of the IBC panel with each cell measured individually (all of the cells on the panel being desoldered from each other and measured one by one under the same beam illumination), in parallel and series connections under varying beam diameter, and thus varying intensity of 1060 nm laser illumination

Connection of Columns	*Beam Diameter (FWHM)*	*Power*	*Intensity*	*Efficiency*
Series	43.9 cm	15.0 W	99.2 W/m^2	7.95%
Series	43.9 cm	20.0 W	140.7W/m^2	8.66%
Series	53.3 cm	20.0 W	89.5 W/m^2	8.34%
Series	53.3 cm	25.0 W	106.0W/m^2	7.91%
Parallel				3.66%
Columns Individual Sum				9.22%
Series	53.3 cm	30.1 W	131.0W/m^2	7.69%
Series	53.3 cm	35.3 W	157.0W/m^2	7.73%
Series	53.3 cm	40.0 W	180.0W/m^2	7.01%
Series	53.3 cm	45.1 W	202.0W/m^2	7.04%
Series	53.3 cm	50.0 W	225.0W/m^2	6.01%
Individual Cells Sum	32.3 cm	50.0 W	610.0 W/m^2	18.4%
Individual Cells Sum	21.9 cm	50.0 W	1327.0 W/m^2	19.0%

At 25 W and 53.3 cm beam diameter, the parallel connection of the columns was providing 3.70 A short circuit current and 0.64 V open circuit voltage and with such a high current the resistance of the cables connecting the panel to the measurement system were showing great ohmic behavior in the IV curves of those measurements. Thus, it was not feasible to measure with parallel connections at high powers. So, it was continued with series connections of the columns or individual cell measurements at high powers. At 50 W of power the series connection of the columns was providing 2.42 A short circuit current and 3.30 V open circuit voltage.

Measurements started with 43.9 cm FWHM with 15 W power providing 7.95% efficiency with series connection of the columns. As the power was increased to 20 W, efficiency reached 8.66%. Then, increasing the beam diameter to 53.3 cm resulted in a lower efficiency (8.34%). Increasing the power for obtaining the same intensity was tried however it resulted in even a lower efficiency (7.91%). Under the same beam, changing the connection to parallel provided 3.66% and measuring each cell individually and summing up their efficiencies at their MPPs resulted in 9.22%. Then continuing with series connection, as the beam power was increased until 50 W, efficiency decreased until 6.01%. When the beam diameter was set to 32.3 cm with 50 W and each cell was individually measured, the sum of efficiencies resulted in 18.4%. This has risen to 19.0% as the beam diameter was decreased to 21.9 cm.

The efficiency distribution of each cell for the 32.3 cm beam diameter is presented in Figure 5.19(a) together with the 3D graph of efficiency with respect to location on the panel (Figure 5.19(b)). The individual measurement efficiencies were calculated with respect to the incident 50 W.

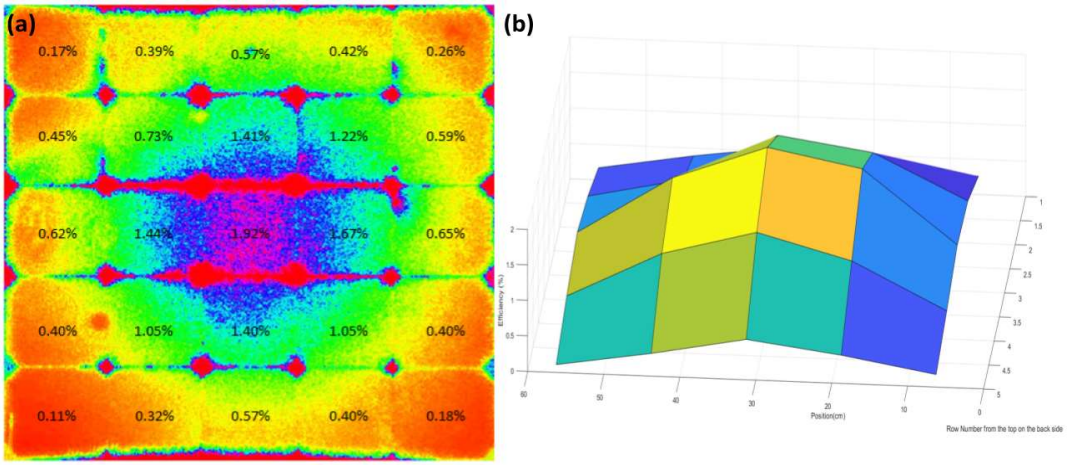

Figure 5.19. (a) Distribution of efficiency with respect to 50 W of incident power over the IBC Panel and (b) The 3D graph of that distribution with z-axis representing efficiency and x-y axis representing the 2D plane of the panel

Figure 5.20 shows that the power generation is not homogenous across the panel but proportional to the gaussian distribution of the beam. When the short circuit current and the open circuit voltage of the cell in the center which has the highest efficiency measured under this beam configuration, it is seen to be providing 2.65 A and 0.70 V, generating 0.96 W at its maximum power point. Comparing this intensity to the highest single IBC cell measurement (Figure 5.18(b)) that provided 40.3% efficiency, it is seen that the center cell is receiving too much power with respect to the ideal case. Ideal case had incident 2.0 W of 1050 nm light and near 5500 W/m^2 intensity. Its beam diameter was approx. 1.6 cm and generating 0.80 W of electrical power at its maximum power point. Its short circuit current and the open circuit voltage was 1.67 A and 0.68 V respectively. Comparing the short circuit currents, the cell on the panel with this beam is receiving too much power with respect to the ideal measurement results previously obtained with single cell.

At the same time, the cells near the edges and corners of the panel are receiving relatively low powers. The corner with lowest efficiency (0.11%) located on the most bottom left had I_{sc} 0.16 A and V_{oc} 0.63 V, generating 0.059 W at its MPP. So, the Gaussian distribution of the laser beam is limiting the efficiency at this step along

with; the intensity, the beam area, and the total power incident to each cell being non-ideal.

The usage of I_{sc} for comparing incident power and cell performance can be verified by the observations on Figure 5.20. It shows that the efficiency and short circuit currents of the cells are proportional to each other. When a gaussian fit is made to the short circuit currents of the center row and normalized, the graph obtained is very similar to the normalized gaussian beam profile of the incident beam intensity, as can be seen in Figure 5.20. So, the short circuit current comparison is an effective way to comment on the behavior of the cells under a certain beam configuration.

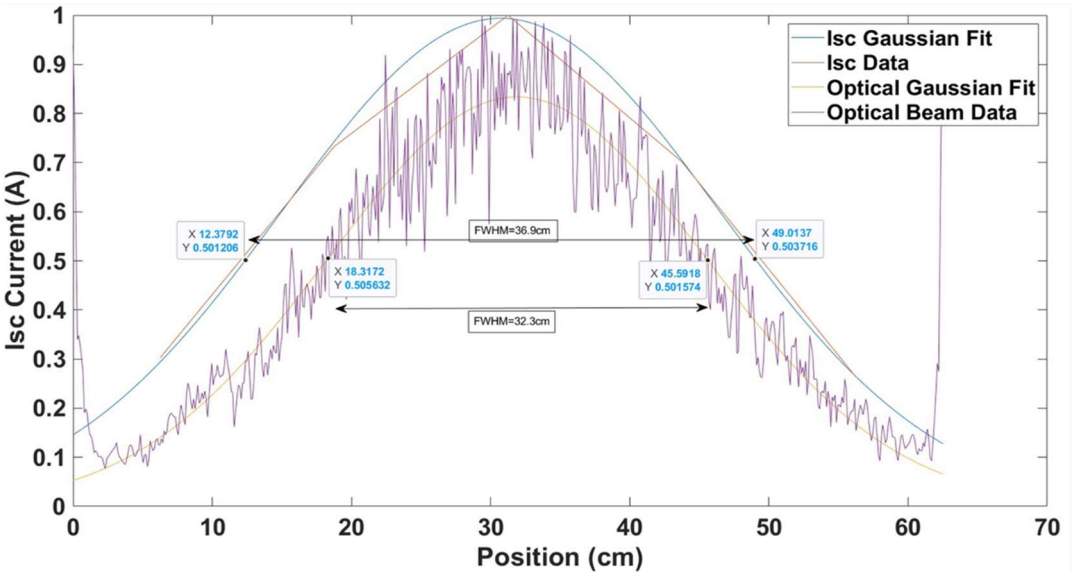

Figure 5.20. Normalized short-circuit current (Isc) and normalized beam power with respect to position

The gaussian beam profile power can also be inspected by equation 5.1. The calculated values are illustrated in Figure 5.21 for the 50 W power with FWHM beam diameter 53.3 cm and 32.3 cm. For the 53.3 cm FWHM beam diameter, a radius of 12.5/2 cm (which is half of the side length of an IBC cell) is receiving 14.14% of the total power which is 7.07 W. A radius of 37.5/2 cm (half of the side length of 3 IBC cells) is receiving 74.65% of the total power which is 37.33 W. When the center cell

power is subtracted, there is 30.26 W divided by 9 cells, each receiving 3.78 W. Then the radius 62.5/2 cm (half of the panel length) receiving 97.79% power.

Similarly, for the 32.3 cm FWHM beam diameter, a radius of 12.5/2 cm is receiving 33.98% of the total power which is 16.99 W. A radius of 37.5/2 cm is receiving 97.62% of the total power which is 48.81 W. When the center cell power is subtracted, there is 31.82 W divided by 9 cells, each receiving 3.98 W. Then the radius 62.5/2 cm (half of the panel length) receiving 99.9968% power. So, the panel is receiving approx. 100% of the power sent in each case.

As it can be seen that some of the cells are receiving too much power with respect to the power they have performed their best efficiency (which was under 2 W of power resulting in approx. 40% efficiency) while others near the edge receive very less power. If the beam is enlarged for distributing power more evenly, then a considerable amount will be lost at the edges being not incident to the panel in the first place.

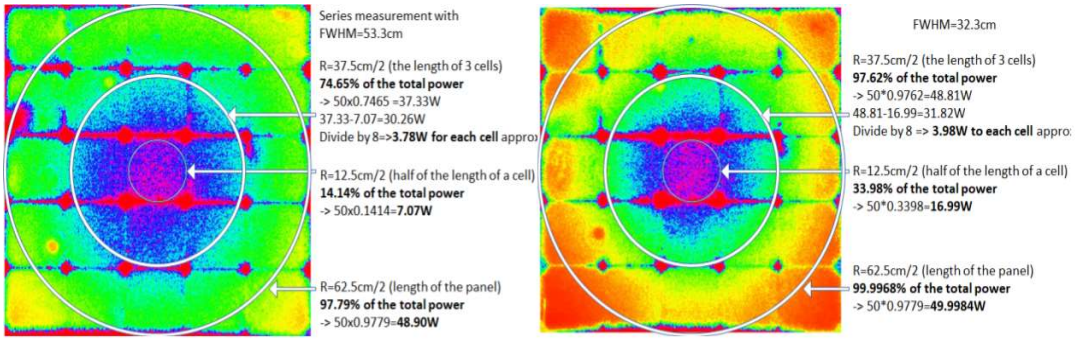

Figure 5.21 Power distribution of a gaussian profile beam with 50 W labeled on colormap image for FWHM=53.3 cm (on the left) and FWHM=32.3 cm (on the right)

Thus, for a design of a power beaming receiver with ideal power conversion, in order to meet all the necessary criteria; ideal intensity, ideal beam area, ideal total power incident to each single cell and homogeneity of the beam power needs to be in consideration. A multi-beam approach can be applied which can be meeting all these criteria at the same time, providing ideal power, ideal beam area and ideal intensity to each single beam, raising the efficiency to much higher levels.

Another experiment that was conducted is, soldering four IBC cells in a series connection forming a 2x2 panel. The purpose was to see if the efficiency can be increased by decreasing the area on the cell while at the same time minimizing the ohmic losses in the connection cables and connectors used on the panel. So, the connections were made with the shortest length possible. It did indeed increase the efficiency up to 22.4% at 10 W of power. However, it was not possible to increase efficiency after that value either by changing the power of the beam, or the beam area. This experiment was conducted by using 1050 nm light and the results can be seen in Table 5.5. As it can be observed again that the efficiency does not have a linear relationship with either power or the intensity. The measurement started with 11.5 cm beam diameter and 8W of 1050 nm power providing 13.0% efficiency. The power was increased until the efficiency starts to decrease. The peak efficiency was at 14.8% under 10 W. Then the beam diameter was decreased to 8.4 cm, increasing the intensity but this did not increase the efficiency. Then increasing the beam diameter to 12.7 cm was experimented, decreasing the intensity. This resulted in 21.6% efficiency and when the intensity was lowered even further, until 10W, the peak efficiency of 22.4% was obtained.

Table 5.5 Efficiency of the 4 IBC cells connected in series under varying beam diameter and thus varying intensity of 1050 nm laser illumination

Beam Diameter (FWHM)	*Power*	*Intensity*	*Efficiency*
11.5 cm	8 W	768 W/m^2	13.0%
11.5 cm	10 W	1014 W/m^2	14.8%
11.5 cm	13 W	1860 W/m^2	13.6%
8.4 cm	13 W	2329 W/m^2	13.7%
12.7 cm	13 W	1026 W/m^2	21.6%
12.7 cm	17 W	1342 W/m^2	20.6%
12.7 cm	15 W	1184 W/m^2	21.2%
12.7 cm	10 W	790 W/m^2	22.4%
12.7 cm	8 W	632 W/m^2	21.6%

Thus, minimizing the cable connections improved the efficiency while connecting 4 cells in series also enabled greater power transmission with less current, thus less ohmic losses. So, it can be concluded that the series connection is more feasible for high powers than parallel connections.

5.7 Long Distance Field Experiment

In this section, the findings of a long-distance field experiment are presented. The obstacles and the results of the field experiment are discussed. In a remote area inside METU campus, two types of PV cell structures; IBC and thin multi-cell (stack of bifacial PERC cells) were placed at a distance of approximately 100 m from the laser system.

In order to achieve the beam diameter needed at the focus point (BDAF) at 100 m, an adjustment to the laser setup has been made by mounting an additional external lens. However, since this second lens did not have an anti-reflection coating for IR, it was a factor causing lower efficiency than what is possible.

Also, during transportation to the experiment location, one of the cells in the multi-cell design got broken (G5 the frontest and the thinnest cell). Due to this, measurements were done without the frontest cell of the multi-cell design with only four cells remaining. The laser was tuned to 1060 nm, providing 5 W of power and the beam diameter was approximately 7 cm.

The thin multi-cell stack with only 4 cells remaining has provided 8.72% efficiency when cells were connected in parallel with approx. 100 m distance. The IBC cell has provided 12.9% efficiency. A black cardboard was placed behind the cell, providing shadow from the sun so that sunlight does not add any discrepancy to the measurement. The setup visual can be observed in Figure 5.22.

Figure 5.22. An image of the thin multi-cell stack being used in the field

The obtained result with the thin multi-cell stack is very close to the best efficiency values obtained in the laboratory (near 8% with 1060nm). However, the IBC efficiency is relatively low with respect to single cell measurements in the laboratory. The reason for this can be the change of beam shape that was observed with an IR camera on the experiment area. As it can be seen on Figure 5.23, the beam shape was consisting of concentric rings. The reason for this was realized to be the fiber endcap that was made soon before the field experiment. While working at 50 W, the fiber tip got burned and a fiber endcap was made in order to avoid it. However, the concentric ring shape was not observed in the short range inside the laboratory.

Figure 5.23. IR image of the laser beam taken at the field experiment

The non-homogeneity of the beam is anticipated to lower the efficiency. Its effect may be negligible on the thin multi-cell stack due to the already present high rate of scattering on the cells. On the other hand, IBC cell's reaction to non-homogeneity of the beam is much greater as observed in the double beam experiment. Thus, the efficiency can be higher when the endcap is removed and an angled cleave made again to the fiber tip as it was throughout all the single cell measurements before 50 W measurements.

Due to the equipment limitation in the experiment area, the lens was not able to be adjusted to have a beam diameter of 1.6 cm which has resulted with the highest efficiency in single cell measurement of IBC cell. Since the beam diameter was approximately 7 cm in addition to having a non-homogeneous shape, the beam parameters were far from ideal for the IBC cell. With these non-ideality factors, the additional lens that was introduced for beam focusing was causing 8% loss of power due to not having an anti-reflection IR coating. The power measured before the additional lens due to beam size being greater than the powermeter's light entrance after the additional lens.

Hence the results of field experiment can be improved by removing the fiber endcap of the fiber laser system, changing the additional lens with an anti-reflection coated one for IR, adjusting the beam diameter to the ideal length for the cells and repeating the experiments with these changes.

CHAPTER 6

CONCLUSION

Within the scope of this study, a laser system with a tunable wavelength ranging from 1030 nm to 1080 nm was designed and fabricated. To the best of our knowledge, no prior studies in the field of power beaming have incorporated a wavelength-tunable laser. While some studies have examined lasers of different wavelengths, none have demonstrated the ability to precisely adjust the wavelength to a chosen value, particularly near the bandgap energy of the receiver material. The laser system developed was capable of delivering more than 50 W of power and could be collimated and directed over long distances as required.

Numerical simulations were conducted for both monofacial and bifacial Passivated Emitter and Rear Contact (PERC) cells. The simulated designs were fabricated and studied under the simulated wavelengths, and methods for achieving the predicted efficiency were discussed.

Furthermore, a novel thin multi-cell stack of bifacial PERC cells was introduced and examined under various beam powers, beam diameters, and wavelengths. Additionally, the Interdigitated Back Contact (IBC) structure was investigated under the same parameters varying. To the best of our knowledge, no previous studies have explored the use of the IBC structure in the context of power beaming. A photovoltaic (PV) panel incorporating IBC cells was constructed and evaluated under different beam parameters.

Finally, a long-distance field experiment was conducted outdoors. The results, along with the challenges encountered, were analyzed. There are still many areas that needs further investigation related to the concept of power beaming presented in this project. On a global scale, research in power beaming remains limited, and existing research groups often do not disclose detailed information about their systems. This

is likely due to strategic concerns while the technology being just starting to gain attention.

All in all, many findings have been obtained for designing a photovoltaic receiver for power beaming applications regarding the behavior of a photovoltaic cell under a specific power, area and intensity in addition to the information gained about the obstacles that will be faced while conducting field experiments. Future work includes, as mentioned in the related sections; a holder with cooling function and decreased space between cells for improved light transmission and less scattering needs to be designed for the thin multi-cell stack, study on impedance calculations for the PV cells' local regions and investigation over simulations the effect of non-homogenous illumination of the cells, and implementation of a cooling system on the IBC cell mounted on an aluminum plate.

REFERENCES

1. Tesla, N. (1891), Experiments with alternate currents of very high frequency and their application to methods of artificial illumination, Trans. Am. Inst. Electr. Eng., 8(1), 266–319.
2. Triviño, A., González-González, J. M., & Aguado, J. A. (2021), Wireless power transfer technologies applied to electric vehicles: A review, Energies, 14(6), 1547.
3. Iyer, V., Bayati, E., Nandakumar, R., Majumdar, A., & Gollakota, S. (2017), Charging a smartphone across a room using lasers, Proc. ACM Interact. Mob. Wearable Ubiquitous Technol., 1(4), 143.
4. Achtelik, M. C., et al. (2011), Design of a flexible high performance quadcopter platform breaking the MAV endurance record with laser power beaming, 2011 IEEE/RSJ Int. Conf. Intell. Robots Syst., 5166–5172
5. Glaser, P. E., et al. (1974), Feasibility study of a satellite solar power station, NASA, Rep. No. ADL-C-74830.
6. Fuada, S., et al. (2024), Study on fat as the propagation medium in optical-based in-body communications, Nordic Conference on Digital Health and Wireless Solutions, Cham: Springer Nature Switzerland, 179–190.
7. Miyamoto, T. (2024), Optical WPT, in Theory and Technology of Wireless Power Transfer, CRC Press, 179–245.
8. Raible, D. E., Dinca, D., & Nayfeh, T. H. (2011), Optical frequency optimization of a high intensity laser power beaming system utilizing VMJ photovoltaic cells, Proc. 2011 Int. Conf. Space Opt. Syst. Appl. (ICSOS).
9. "Abundance of elements in the Earth's crust and in the sea," (2016–2017), CRC Handbook of Chemistry and Physics, 97th ed., sec. 14, p. 17.
10. Brown, W. (1964), Experiments in the transportation of energy by microwave beam, 1958 IRE Int. Conv. Rec., 8–17.
11. Brown, W., Mims, J., & Heenan, N. (1965), An experimental microwave-powered helicopter, 1958 IRE Int. Conv. Rec., 225–235.

12. Glaser, P. E. (1968), Power from the sun: Its future, Science, 162(3856), 857–861.
13. Ayling, A., Fikes, A., Mizrahi, O. S., Wu, A., Riazati, R., Brunet, J., Abiri, B., Bohn, F., Gal-Katziri, M., Hashemi, M. R. M., Padmanabhan, S., Russell, D., & Hajimiri, A. (2024), Wireless power transfer in space using flexible, lightweight, coherent arrays, Acta Astronautica, 224, 226–243
14. Brown, W. C. (1996), The history of wireless power transmission, Solar Energy, 56(1), 3–21.
15. Von Ramm, O. T., & Smith, S. W. (1983), Beam steering with linear arrays, IEEE Trans. Biomed. Eng., BME-30(8), 438–452.
16. Green, M. A., Blakers, A. W., Zhao, J., & Wang, A. (1992), 45% efficient silicon photovoltaic cell under monochromatic light, IEEE Electron Device Lett., 13(6), 317–318
17. Green, M. A. (2001), Limiting photovoltaic monochromatic light conversion efficiency, Prog. Photovolt. Res. Appl., 9(4), 257–261
18. Takeda, K., Tanaka, M., Miura, S., Hashimoto, K., & Kawashima, N. (2002), Laser power transmission for the energy supply to the rover exploring ice on the bottom of the crater in the lunar polar region, Proc. SPIE, 4632, 223–227
19. Blackwell, T. (2005), Recent demonstrations of laser power beaming at DFRC and MSFC, AIP Conf. Proc., 766(1), 129–136.
20. Kawashima, N., Takeda, K., & Yabe, K. (2012), Possible utilization of the laser energy transmission in space, Trans. Jpn. Soc. Aeronaut. Space Sci., Aerosp. Technol. J., 10(ISTS28).
21. Summerer, L., & Purcell, O. (2009), Concepts for wireless energy transmission via laser, ESA-Advanced Concepts Team.
22. He, T., et al. (2014), High-power high-efficiency laser power transmission at 100 m using optimized multi-cell GaAs converter, Chinese Phys. Lett., 31(10), 104203.

23. Nugent, T., & Kare, J. (2010), Lasermotive white paper: Power beaming for UAVs.
24. Abdelhady, A. M., et al. (2024), Operation optimization of laser-powered aerial data harvesting for passive IoT networks, 2024 IEEE Wireless Commun. Netw. Conf. (WCNC).
25. Lim, Y., Choi, Y. W., & Ryoo, J. (2021), Study on laser-powered aerial vehicle: Prolong flying time using 976 nm laser source, 2021 International Conference on Information and Communication Technology Convergence (ICTC), 1220–1225.
26. Jaffe, M., Vaughan, K. N., & Mankins, V. (2012), SPS-ALPHA: The first practical solar power satellite via arbitrarily large phased array (a 2011–2012 NIAC project), 10th International Energy Conversion Engineering Conference, 3978.
27. Mankins, J. (2014), The case for space solar power, Houston, TX, USA: Virginia Edition Publishing.
28. Sasaki, S., et al. (2004), Conceptual study of SSPS demonstration experiment, URSI Radio Science Bulletin, (310), 9–14.
29. International Union of Radio Science, et al. (2007), URSI White Paper on Solar Power Satellite (SPS) Systems and Report of the URSI Inter-Commission Working Group on SPS, URSI-International Union of Radio Science.
30. Zheng, Y., Zhang, G., Huan, Z., Zhang, Y., Yuan, G., Li, Q., Ding, G., Lv, Z., Ni, W., Shao, Y., Liu, X., & Zu, J. (2024), Wireless laser power transmission: Recent progress and future challenges, Space Solar Power and Wireless Transmission, 1, 17–26.
31. Küblböck, M., Will, J., & Fattahi, H. (2024), Solar lasers: Why not?, APL Photonics, 9(5), 050903.
32. Abdullah, S., Mulles, P. J. S., & Amaya, R. E. (2022), A new adaptive wireless power transfer solution for use with space rovers and vehicles,

2022 IEEE International Conference on Wireless for Space and Extreme Environments (WiSEE), 49–54.
33. Sanders, M., and J. S. Kang (2020), Utilization of polychromatic laser system for satellite power beaming, 2020 IEEE Aerospace Conference, 1–7.
34. Kerslake, T. W. (2008), Lunar surface-to-surface power transfer, AIP Conf. Proc., 969, 466–473.
35. Oubei, H. M., Li, C., Alouini, M.-S., & Ooi, B. S. (2015), 4.8 Gbit/s 16-QAM-OFDM transmission based on compact 450-nm laser for underwater wireless optical communication, Opt. Express, 23(18), 23302–23309.
36. Chen, Y., Kong, M., Tang, A., Wang, J., Shi, R., Huang, J., Guo, C., Shi, B., Deng, N., & Xu, J. (2017), 26 m/5.5 Gbps air-water optical wireless communication based on an OFDM-modulated 520-nm laser diode, Opt. Express, 25(13), 14760–14765.
37. Wu, T.-C., Chi, Y.-C., Wang, H.-Y., Tsai, C.-T., & Lin, G.-R. (2017), Blue laser diode enables underwater communication at 12.4 Gbps, Sci. Rep., 7, 40480.
38. Wang, J., Lu, C., Li, S., & Xu, Z. (2019). 100 m/500 Mbps underwater optical wireless communication using an NRZ-OOK modulated 520 nm laser diode. Optics Express, 27(9), 12171–12181.
39. Zhu, S., Chen, X., Liu, X., Zhang, G., & Tian, P. (2020), Recent progress in and perspectives of underwater wireless optical communication, Prog. Quantum Electron., 73, 100274.
40. Pradhan, P., Ghosh, M., & Majumder, A. (2022), Effect of transmitter divergence-angle on the performance of underwater visible light communication system, Opt. Quant. Electron., 54(12), 802.
41. Chen, X., Liu, W., Chen, Y., Yang, Q., Sun, S., Zhang, Z., Ma, X., Chen, L. (2019), Diversity-reception UWOC system using solar panel array and maximum ratio combining, Opt. Express, 27(23), 34284–34297.

42. Fadel, J., Tabassum, A., Oubei, H., Alouini, M., & Schull, S. (2020), Toward self-powered internet of underwater things devices, IEEE Commun. Mag., 58(1), 68–73.
43. Al-Hameed, S., Al-Kinani, A., Mohammed, A., & Sait, S. (2022), Energy-aware underwater optical system with combined solar cell and SPAD receiver, IEEE Commun. Lett., 26(1), 59–63.
44. Miskin, M. Z., et al. (2020), Electronically integrated, mass-manufactured, microscopic robots, Nature, 584, 557–561.
45. Ahnood, A., et al. (2020), Miniature power and data transceiver based on multimodal operation of a single photovoltaic device, Engineering Research Express, 2, 015036.
46. Fafard, S., & Masson, D. P. (2021), Perspective on photovoltaic optical power converters, J. Appl. Phys., 130(16), 160901.
47. Fafard, S., & Masson, D. P. (2022), High-efficiency and high-power multijunction InGaAs/InP photovoltaic laser power converters for 1470 nm, Photonics, 9(7), 438.
48. Helmers, H., Höhn, O., Lackner, D., López, E., Ruiz-Preciado, L., Schauerte, M., Siefer, G., Dimroth, F., and Bett, A. W. (2019), Highly efficient III-V based photovoltaic laser power converter, 1st Optical Wireless and Fiber Power Transmission Conf. (OWPT2019), no. OWPT-1-01, Yokohama, Japan.
49. Jaffe, P., Nugent, T., Strassner II, B., & Szazynski, M. (2024), Power Beaming: History, Theory, and Practice, World Scientific Publishing Company, 420 pp., ISBN: 978-981-124-310-3.
50. Green, M. A. (2007), Thin-film solar cells: Review of materials, technologies, and commercial status, J. Mater. Sci. Mater. Electron., 18(S1), 15–19.
51. Geist, Jon, Warren K. Gladden, and Edward F. Zalewski. "Physics of photon-flux measurements with silicon photodiodes." Journal of the Optical Society of America 72.8 (1982): 1068-1075.

52. Silfvast, W. T. (2008), Laser Fundamentals (2nd ed.), Cambridge University Press, p. 2.
53. i Ponsoda, J. J. M. (2013), "Analysis of photodarkening effects in ytterbium-doped laser fibers.".
54. Smets, A., Jäger, K., Isabella, O., van Swaaij, R., & Zeman, M. (2016), Solar Energy: The Physics and Engineering of Photovoltaic Conversion, Technologies and Systems, Bloomsbury Publishing, p. 48-159.
55. Würfel, P. (2005), Physics of Solar Cells: From Principles to New Concepts, Wiley-VCH, p. 113.
56. Conibeer, G. (2007), Third-generation photovoltaics, Mater. Today, 10(11), 42–50.
57. Bludau, W., Onton, A., & Heinke, W. (1974), Temperature dependence of the band gap of silicon, J. Appl. Phys., 45(4), 1846–1848.
58. de Vos, A. (2008), Thermodynamics of Solar Energy Conversion, Wiley-VCH, p. 135.
59. Richter, A., Hermle, M., & Glunz, S. W. (2013), Reassessment of the limiting efficiency for crystalline silicon solar cells, IEEE Journal of Photovoltaics, 3(4), 1184–1191.
60. Bader, S., Ma, X., & Oelmann, B. (2019), One-diode photovoltaic model parameters at indoor illumination levels–A comparison, Solar Energy, 180, 707–716.
61. Rizzo, L., et al. (2020), Comparison of terahertz, microwave, and laser power beaming under clear and adverse weather conditions, Journal of Infrared, Millimeter, and Terahertz Waves, 41, 979–996.
62. Ptashnik, I., McPheat, R., Shine, K. (2011), Water vapor self-continuum absorption in near-infrared windows derived from laboratory measurements, Journal of Geophysical Research: Atmospheres, 116, D16305.

63. Beaumont, B., et al. (1991), High efficiency conversion of laser energy and its application to optical power transmission, Proceedings of the 22nd IEEE Photovoltaic Specialists Conference, Las Vegas, NV, 997–1000.
64. MacDougal, M. H., et al. (1995), Ultralow threshold current vertical-cavity surface-emitting lasers with AlAs oxide-GaAs distributed Bragg reflectors, IEEE Photonics Technology Letters, 7, 229–231.
65. Joyce, W. B., et al. (1996), High-power selectively oxidized vertical-cavity surface-emitting lasers, Quantum Electronics and Laser Science Conference, Anaheim, CA, 80–81.
66. Konno, S., Yasui, K. (1998), Efficient high-power green beam generation by use of an intracavity frequency-doubled laser-diode-pumped Q-switched Nd:YAG laser, Applied Optics, 37, 551–554.
67. Kim, K. S., et al. (2006), 1060 nm vertical-external-cavity surface-emitting lasers with an optical-to-optical efficiency of 44% at room temperature, Applied Physics Letters, 88, 091107.
68. Seurin, S. P., et al. (2008), High-power high-efficiency 2D VCSEL arrays, Proceedings of SPIE 6908, Vertical-Cavity Surface-Emitting Lasers XII, San Jose, CA, 690808.
69. Bruesselbach, H., et al. (2012), 106 W continuous-wave output power from vertical-external-cavity surface-emitting laser, Electronics Letters, 48, 516–517.
70. Martini, R., et al. (2013), Fiber-coupled high-power diode-lasers with highest radiance, Proceedings of the 2013 High Power Diode Lasers and Systems Conference (HPD), Coventry, UK, 36–39.
71. Xin, D., et al. (2009), All-solid-state Nd:YAG laser operating at 1064 nm and 1319 nm under 885 nm thermally boosted pumping, Chinese Physics Letters, 26, 094207.
72. Malyutenko, N., et al. (2020), Continuous-wave dual-wavelength operation of the in-band diode-pumped Nd:GdVO4/Nd:YVO4 composite laser with controllable spectral power ratio, Applied Physics B, 126, 75.

73. Jiang, D., et al. (2018), High order cascaded Raman random fiber laser with high spectral purity, Optics Express, 26, 5275–5280.
74. Yang, L., et al. (2022), 48 W continuous-wave output from a high-efficiency single emitter laser diode at 915 nm, IEEE Photonics Technology Letters, 34, 1218–1221.
75. Eilchi, M., & Parvin, P. (2016), Gain saturation in optical fiber laser amplifiers, in Fiber Laser, IntechOpen, pp. 297–320.
76. Lin, M., et al. (2021), Intrinsic losses in photovoltaic laser power converters, Applied Physics Letters, 118(10).

APPENDICES

A. Custom Built IV Measurement and PV Cell Characterization System

The photovoltaic cells were needed to be experimented with under different optical parameters (beam power, area, etc.). So, an IV measurement system was built which allows the current to increase incrementally. At each increment, the voltage and current of the photovoltaic cell is measured which becomes one data point of the IV curve. When all of the incremental data points are plotted, the complete IV curve of the cell under that specific optical parameters are obtained (Figure A.3(b)). From the IV curve of a cell, its maximum power point (MPP) can be found and the highest efficiency it can provide under the specific parameters can be determined. For this purpose, a measurement system that incrementally changes the gate voltage of a logic-level MOSFET was designed. As the MOSFET's gate is incrementally opened, more current passes, decreasing the voltage of the cell. At each increment the voltage and the current is measured and recorded as a datapoint that will form the complete IV curve when the measurement process is finished. The scheme of the system is shown in Figure A.1.

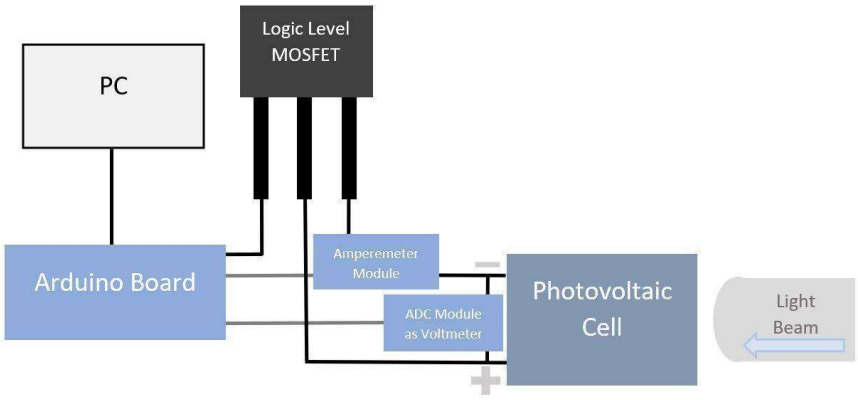

Figure A.1. General scheme of the developed IV measurement setup

An Arduino Uno is used for controlling the components and communicating with a computer. It is obtaining the voltage measurements by controlling a 16-bit Analog-

to-Digital Converter (ADC) and the current module (ACS 724) for measuring the current. The voltage limit is 6.4 V and has ±0.2 mV error while the current limit is 40 A with an error of ±100 mA. The current error is most probably caused by stray magnetic fields since the current module relies on the Hall effect. An overview of the measurement system can be seen in Figure A.2.

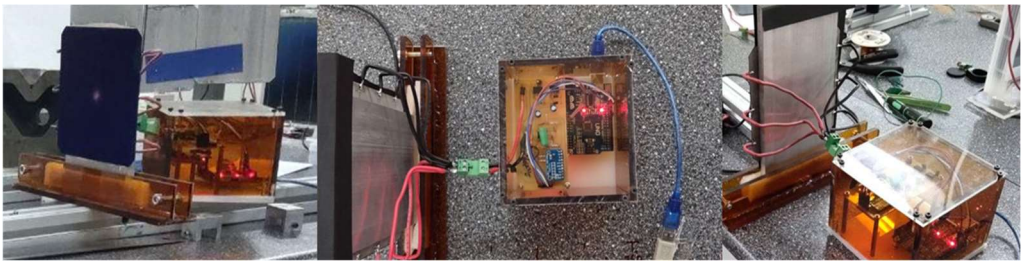

Figure A.2. Images of the measurement system connected to an IBC cell while measurement

An external circuit with a Sallen-Key filter was designed for producing analog output controlled by the Arduino due to Arduino lacking an analog output option. This external circuit was custom designed and printed on a copper plate, later processed with Iron (III) Chloride, drilled for component holes and all the components were soldered on the board. The Sallen-key filter is used to attenuate all high frequencies coming by the PWM pins of Arduino such that only the DC component of the signal is left effectively. The rise time was adjusted so that practically the circuit was providing an analog output which was verified by the aid of an oscilloscope. The Sallen Key Filter schematic can be seen in Figure A.3(a).

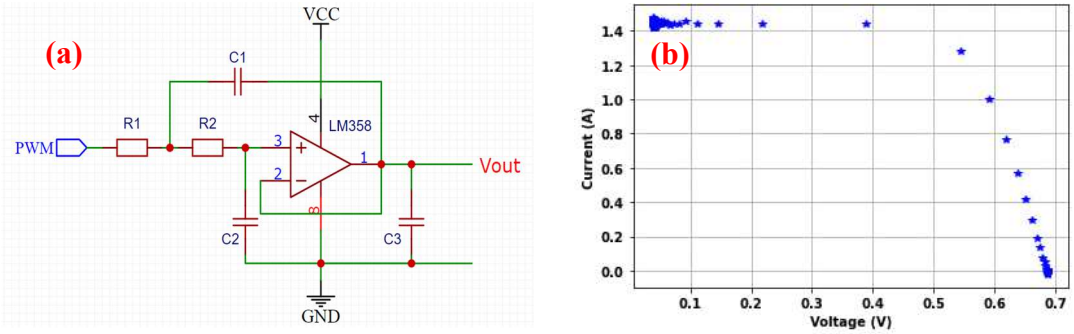

Figure A.3. (a) Sallen-Key low-pass filter topology with unity gain, with general resistor and capacitor values (b) A typical IV curve obtained from measurements

The results of the measurement system were compared and verified with the professional solar simulator in GUNAM using the same solar cell sample under the same illumination. So, it can be concluded that the custom-built PV cell characterization system is accurate with respect to the professional solar simulator used in GUNAM. The complete electronic scheme of the circuit can be seen in Figure A.4.

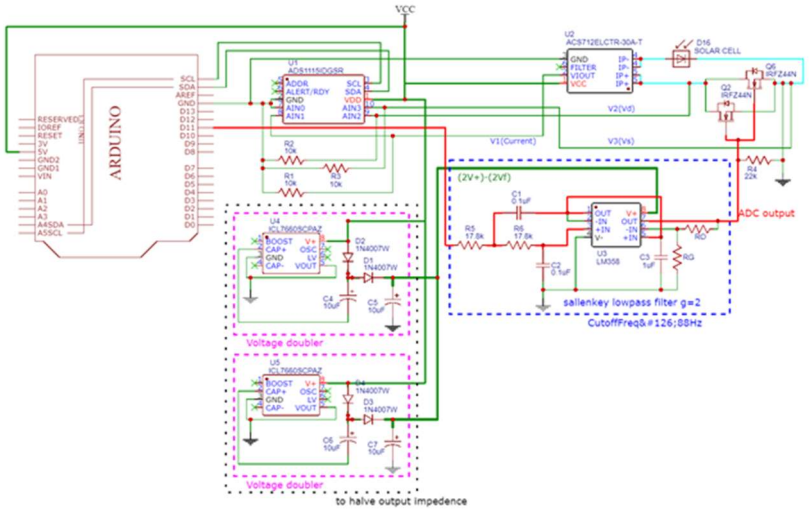

Figure A.4. Full electronical schematic of the improved measurement system

B. Gaussian Beam Diameter Measurement

The beam diameters are measured by the aid of an IR Thorlabs scientific camera. The IR image of the laser beam incident on the cell is taken with the camera. Then the camera image is digitized via a MATLAB code written for this purpose, turning every pixel into a numeric value from 0 to 1, normalizing the level of brightness of the incident light. Then the center line of the beam is plotted on a graph which provides the Gaussian beam profile. Then the full-width at half-maximum (FWHM) values are obtained from the Gaussian profile which is used as the beam diameter throughout the calculations. As long as the camera image does not show a sign of saturation, it can be made sure that the true beam profile is actually the one provided by the camera. Because, if the obtained amplitude of the beam profile has smaller amplitude than the true one, the profile shape will be still preserved, only the amplitude of the shape will change by a constant coefficient. That coefficient is taken into account when adjusting the exposure time of the IR camera, calibrating the amplitude to the same amount of power which the camera's software is fixated for its beam profile tool shown in Figure B.1 (c) along with the rest of the steps shown in Figure B.1 (a,b,d). The exposure time of the camera was adjusted for getting the live intensity plot to a point of non-saturation while still filling the full range intensity scale of the camera. So, the internal calibration of the camera has been the reference point for the Gaussian beam profile extraction. Great attention has been given to this point while taking the IR images and calculating the beam diameters. If the camera were to saturate, it wouldn't be possible to know where the real maximum intensity is and thus what is the FWHM, resulting in an inaccurate beam diameter. Thus, it is ensured this way for not having any discrepancy from the true physical observable.

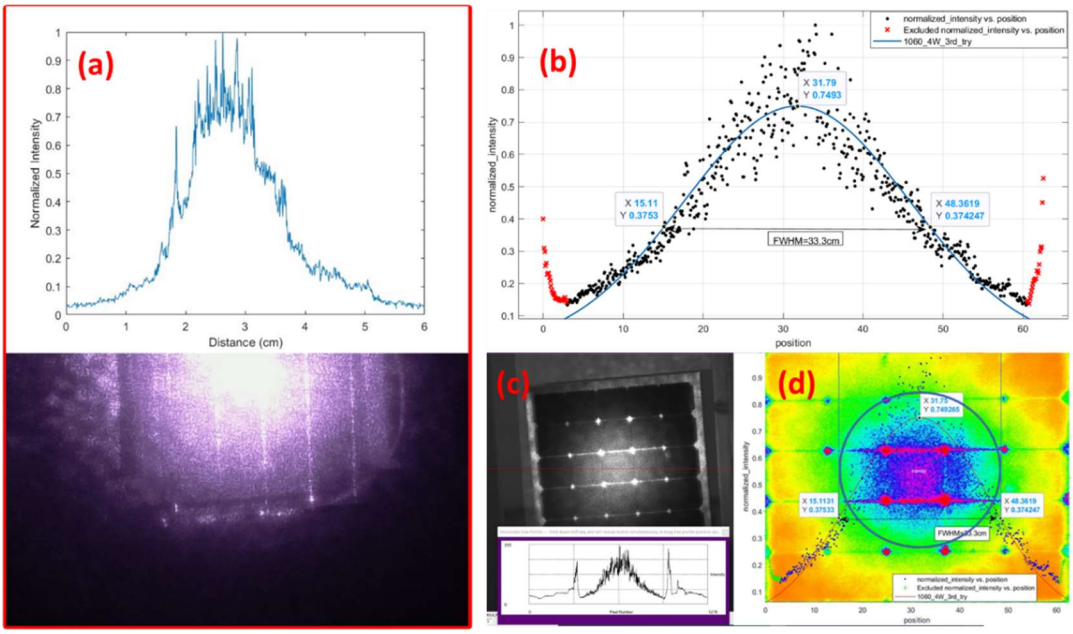

Figure B.1. (a) Gaussian profile obtained from an IR image, the raw image is below the graph (b) The Gaussian Profile data is applied to a Gaussian fit depending on the rate of speckle noise and FWHM beam diameter is obtained (c) An example IR camera image of IBC cell panel with the beam profile tool of camera's software on the bottom (d) Gaussian fit applied to a Gaussian profile obtained by IR image of the IBC panel under laser illumination and colormap of the IR image is placed on the background of the graph with FWHM diameter beam shown by the drawing of a blue circle in the center